


New tool for 21-cm cosmology. I. Probing Λ CDM and beyondJordan Flitter^{*} and Ely D. Kovetz*Physics Department, Ben-Gurion University of the Negev, Beer-Sheva 84105, Israel* (Received 17 September 2023; accepted 18 December 2023; published 9 February 2024)

In this work we present 21cmFirstCLASS, a modified version of 21cmFAST, the most popular code in the literature for computing the inhomogeneities of the 21-cm signal. Our code uses the public cosmic microwave background (CMB) Boltzmann code CLASS, to establish consistent initial conditions at recombination for any set of cosmological parameters and evolves them throughout the dark ages, cosmic dawn, the epoch of heating and reionization. We account for inhomogeneity in the temperature and ionization fields throughout the evolution, crucial for a robust calculation of both the global 21-cm signal and its fluctuations. We demonstrate how future measurements of the CMB and the 21-cm signal can be combined and analyzed with 21cmFirstCLASS to obtain constraints on both cosmological and astrophysical parameters and examine degeneracies between them. As an example application, we show how 21cmFirstCLASS can be used to study cosmological models that exhibit nonlinearities already at the dark ages, such as scattering dark matter (SDM). For the first time, we present self-consistent calculations of the 21-cm power spectrum in the presence of SDM during the nonlinear epoch of cosmic dawn.

DOI: [10.1103/PhysRevD.109.043512](https://doi.org/10.1103/PhysRevD.109.043512)**I. INTRODUCTION**

After a rapid inflationary epoch ended, our Universe continued to expand and cool down. At some point, nearly 400,000 years after the big bang, its temperature was low enough that atoms could first form in a key cosmological moment called *recombination*. Meanwhile, collapsing halos of cold dark matter (CDM) provided the first gravitational seeds for galaxy and star formation. Efficient radiation that was emitted from the first stars and their remnants then ionized the surrounding intergalactic medium (IGM) during the epoch of *reionization* (EoR). Recently on cosmic timescales, the expansion of the Universe has become dominated by the mysterious force of dark energy. This is a brief description of the concordance cosmological model (Λ CDM) [1–4].

Many observables support Λ CDM as being the correct cosmological model of our Universe. Galaxy surveys of our local Universe at redshift $z \lesssim 1$ [5–20], and measurements of the Ly α forest ($z \lesssim 2.5$) [21–25] have found very good agreement between the observed spatial distribution of galaxies and the theoretical predicted distribution. But perhaps it was the cosmic microwave background (CMB) [26–36]—a form of radiation that has been nearly freely propagating since recombination at $z \sim 1100$ —that gave Λ CDM its greatest triumph; measurements of the temperature and polarization anisotropies of the CMB, carried out by the Planck satellite [37] and ground based

experiments [38,39], allowed one to constrain the six parameters of Λ CDM to a subpercent precision level [40].

Despite its success, the Λ CDM model does suffer from tensions with observations (see recent reviews in Refs. [41–44]), and more cosmological data are required to resolve them, especially in the large volume between $2.5 \lesssim z \lesssim 1100$ where our Universe has not been systematically mapped yet. Since according to big-bang nucleosynthesis [45,46] the IGM in our Universe is expected to contain huge amounts of neutral hydrogen before reionization, the 21-cm signal, being sourced by hyperfine energy transitions in hydrogen atoms [47–54], has become an important target for cosmologists.

Nowadays there are ongoing efforts to detect the 21-cm signal by many different collaborations. Some of them focus on detecting the global signal, that is the sky-averaged signal. These include the Experiment to Detect the Global reionization Signature (EDGES) [55], Shaped Antenna measurement of the background Radio Spectrum (SARAS) [56], Large-Aperture Experiment to Detect the Dark Ages [57], the Radio Experiment for the Analysis of Cosmic Hydrogen [58] and Probing Radio Intensity at high-Z from Marion [59]. In addition, radio interferometer telescopes, such as the Giant Metrewave Radio Telescope [60], the Murchison Widefield Array [61], Low Frequency Array [62], the Precision Array for Probing the Epoch of Reionization [63], the Hydrogen Epoch of Reionization Array (HERA) [64] and the Square Kilometre Array [65] are devoted to probing the spatial fluctuations in the signal. While most of these experiments are in the

^{*}jordanf@post.bgu.ac.il

stages of noise calibration and have only placed upper bounds on the amplitude of the power spectrum of the signal, the HERA Collaboration for example has already extracted a meaningful upper bound on the x-ray luminosity of the first stars [66–68] (see also Ref. [69]).

There are several approaches in the literature for computing the anisotropies in the 21-cm signal. One way is to perform full radiative-transfer hydrodynamic simulations, e.g. CoDA [70–72], 21SSD [73] and THESAN [74]. Alternatively, postprocessing of N-body simulations can be applied with ray-tracing algorithms such as C²-RAY [75] or CRASH [76]. While these simulations improved our understanding of the physics of the EoR and helped to refine reionization models, they are computationally expensive and cannot be used for parameter inference. Faster approximated schemes that solve the one-dimensional radiative transfer equation can be found in the codes of BEARS [77], GRIZZLY [78] and BEoRN [79]. There are also approximated purely analytic prescriptions in the literature, e.g. [80]. In Zeus21 [81] the 21-cm power spectrum at $z \gtrsim 10$ can be evaluated in seconds, thanks to an approximated exponential fit that relates the linear matter density fluctuations to the nonlinear fluctuations of the star formation rate density (SFRD). Finally, seminumerical codes that implement the excursion-set formalism [82] are widely used in the literature, from [83] to SimFast21 [84] to the ever-popular 21cmFAST [85,86].

In this paper we introduce our code for calculating the 21-cm anisotropies. We call it 21cmFirstCLASS. It is essentially the merger of the two well-known codes—21cmFAST¹ and the linear Boltzmann solver CLASS² [87]. In this version, the Lyman-Werner (LW) feedback [88–90] as well as the relative velocity between baryons and CDM (V_{cb}) [91–94] are taken into account in each cell, while pop-II and pop-III stars are separated into atomic and molecular cooling galaxies, respectively. In addition, the code contains our past modifications to 21cmFAST to incorporate the Ly α heating mechanism [83,95,96], as well as the ability to consider fuzzy dark matter (FDM) with an arbitrary mass and fraction [97].

There are three main advantages to 21cmFirstCLASS: (1) It generates consistent initial conditions (via CLASS) and thereby allows one to study degeneracies between cosmological parameters and astrophysical parameters. (2) It allows a combined analysis of CMB and 21-cm anisotropies, which improves constraining power and allows for degeneracy breaking. (3) Unlike the standard 21cmFAST code which is designed to begin the simulation at $z = 35$ with a homogeneous temperature field, the user can control the initial redshift of 21cmFirstCLASS, and even set it to recombination. As a consequence, the fields in the box are

evolved nonuniformly from an early redshift, naturally leading to the correct state of the box at $z = 35$. This is particularly important for beyond Λ CDM models which exhibit nonlinear fluctuations early on, e.g. in scenarios with primordial magnetic fields [98].

To demonstrate the last point, we consider as an example an exotic dark matter (DM) model which we refer to as scattering dark matter (SDM). In this model, some part of the dark matter is composed of particles which are able to interact nongravitationally with ordinary matter and scatter off of it elastically [99–124]. In that context, this work resembles the work of Ref. [107], but there are a few important differences. First, Ref. [107] used ARES [125,126] in their astrophysical calculations. This code assumes a simpler astrophysical model than 21cmFAST; it does not account for halo mass dependence in the calculation of the star formation efficiency, and it lacks treatment for star suppression feedbacks in molecular cooling galaxies. Moreover, it computes global astrophysical quantities (e.g. emissivity) from global cosmological quantities (e.g. halo mass function) and therefore does not take into account important nonlinear fluctuations at low redshifts. And secondly, in Ref. [107], the astrophysical parameters were fixed in the analysis, and it focused on the global signal. We on the other hand vary both cosmological and astrophysical parameters and derive forecasts with respect to the 21-cm power spectrum while simulating HERA’s noise. We demonstrate that HERA in its design sensitivity is expected to easily probe SDM with cross sections smaller by an order of magnitude than e.g. forecasted constraints for CMB-S4 [101].

This is not the first work to consider the 21-cm power spectrum in the presence of SDM. However, it is the first work that computes *consistently* the 21-cm power spectrum in the presence of SDM during the nonlinear cosmic dawn epoch. For example, Refs. [102,115,124] have estimated the 21-cm power spectrum by considering only the initial Maxwellian fluctuations in the relative velocity between the SDM and the baryons. In 21cmFirstCLASS, nonlinear fluctuations in the density and the SFRD fields are automatically captured. In follow-up work, we will use 21cmFirstCLASS to extend the work of Ref. [105], which focused on the linear dark ages epoch, to make detailed forecasts for constraining SDM at cosmic dawn.

While working on this project, inspired by the work of Ref. [81] (that introduced the Zeus21 code), we have also studied in detail the impact of early linear fluctuations on the late nonlinear 21-cm power spectrum at low redshifts. The results of that analysis can be found in a companion paper [127] (hereafter referred to as Paper II).

The remaining parts of this paper are organized as follows. In Sec. II we briefly outline the physics of the 21-cm signal. In Sec. III we describe the initial conditions used in our code, and in Sec. IV we compare the output of 21cmFirstCLASS with 21cmFAST. In Sec. V we demonstrate

¹<https://github.com/21cmfast/21cmFAST> (we currently use v. 3.3.1).

²https://github.com/lesgourg/class_public.

how 21-cm and CMB data can be readily combined using 21cmFirstCLASS to relax degeneracies between cosmological parameters. We then move on to discuss the SDM physics and its implementation in 21cmFirstCLASS in Sec. VI. At the end of that section, the results of the SDM evolution and its impact on the 21-cm power spectrum are presented, as well as forecasts for its detectability by HERA. We provide our conclusions in Sec. VII.

Throughout this paper, we adopt the best-fit values for the cosmological parameters from Planck 2018 [40] (without baryon acoustic oscillations), namely we assume a Hubble constant $h = 0.6736$, a primordial curvature amplitude $A_s = 2.1 \times 10^{-9}$ with a spectral index $n_s = 0.9649$, and total matter and baryon density parameters $\Omega_m = 0.3153$, $\Omega_b = 0.0493$. For the CMB calculations we also assume an optical depth to reionization $\tau_{\text{re}} = 0.0544$ and a single species of massive neutrinos with mass $m_\nu = 0.06$ eV. For the fiducial values of the astrophysical parameters in 21cmFAST and 21cmFirstCLASS, we adopt the EOS2021 values listed in Table 1 of Ref. [86]. All of our formulas are expressed in the centimeter-gram-second unit system. To reduce clutter, we often do not explicitly write the independent arguments of the physical quantities (e.g. redshift, wave number, etc.) and they should be inferred from the context.

II. 21cm THEORY

The observed physical quantity of the 21-cm signal is known as the brightness temperature, which reflects the excess or deficit of CMB photons at a given frequency (or redshift),

$$T_{21} = \frac{T_s - T_\gamma}{1 + z} (1 - e^{-\tau_{21}}), \quad (1)$$

where $T_\gamma \propto (1 + z)$ is the redshift-dependent CMB temperature, T_s is the spin temperature, and $\tau_{21} \ll 1$ is the 21-cm optical depth (see classic reviews of the 21-cm signal in Refs. [47,48,50–52]). The spin temperature is a characteristic property of the IGM that measures the relative abundance of hydrogen atoms in the triplet and singlet states, in which the spins of the proton and the electron are aligned and antialigned, respectively. As the Universe evolves, various processes excite the hydrogen gas and compete between themselves on setting the value of the spin temperature. In thermal equilibrium the spin temperature reads as

$$T_s^{-1} = \frac{x_{\text{CMB}} T_\gamma^{-1} + x_{\text{coll}} T_k^{-1} + \tilde{x}_\alpha T_\alpha^{-1}}{x_{\text{CMB}} + x_{\text{coll}} + \tilde{x}_\alpha}. \quad (2)$$

Here, T_k is the IGM gas kinetic temperature, $T_\alpha \approx T_k$ is the color temperature of Ly α photons, and $x_{\text{CMB}} = (1 - e^{-\tau_{21}})/\tau_{21} \sim 1$, x_{coll} and \tilde{x}_α are the CMB [95], collisional [51], and Ly α [128] couplings, respectively.

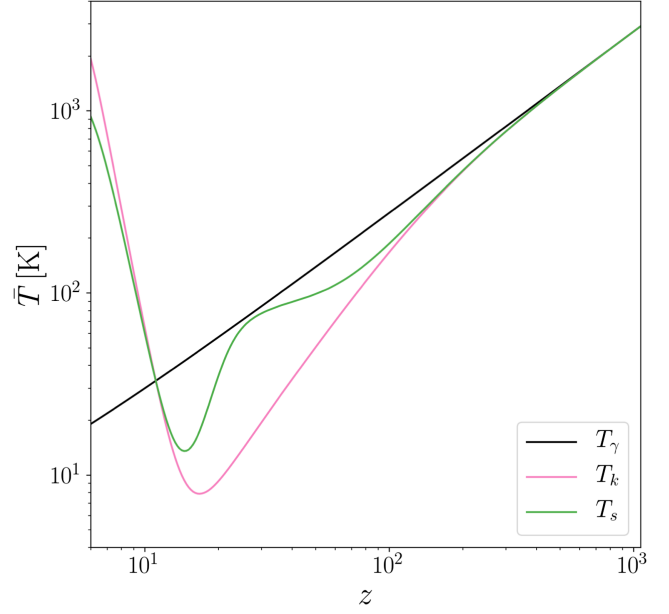


FIG. 1. The evolution of the globally averaged CMB temperature, gas kinetic temperature and the spin temperature. This figure was made with 21cmFirstCLASS.

As we demonstrate in Fig. 1, the globally averaged value of the spin temperature changes with time. Not long after recombination, at $z \sim 1000$, $T_s \approx T_k \approx T_\gamma$. As the Universe expands, the gas adiabatically cools, and its temperature departs from the CMB temperature, and so the spin temperature settles on an intermediate value, which is determined by the ratio of x_{coll} and x_{CMB} . Since x_{coll} is inversely proportional to the volume of the Universe, $x_{\text{coll}} > 1$ at $z \gtrsim 100$, and T_s approaches T_k . Afterward, the Universe becomes large enough so that collisional excitations are no longer efficient, $x_{\text{coll}} < 1$, and T_s is driven back toward T_γ . As can be seen in Fig. 2, the departure of T_s from T_γ at $25 \lesssim z \lesssim 700$ results in the first absorption feature in the globally averaged brightness temperature. This cosmological epoch is known as the *dark ages*. It should be stressed that during this epoch stars have not been formed yet, and therefore the signal is completely determined from cosmology. Hence, within the standard model paradigm, the 21-cm dark ages signal is considered to be well understood theoretically, although it has yet to be measured at that epoch.

The theoretical uncertainty in the 21-cm signal begins after $z \sim 25$, once the first stars have been formed. Ly α radiation emitted from the first stars strongly couples the spin temperature back to T_k via the Wouthuysen-Field (WF) effect [129,130], and a second absorption feature in the 21-cm signal is expected to be found, although its exact shape and location depend on the assumed astrophysical model and are thus highly uncertain. This epoch is known as *cosmic dawn*. Depending on the astrophysical parameters, x rays emitted from stars may heat the surrounding

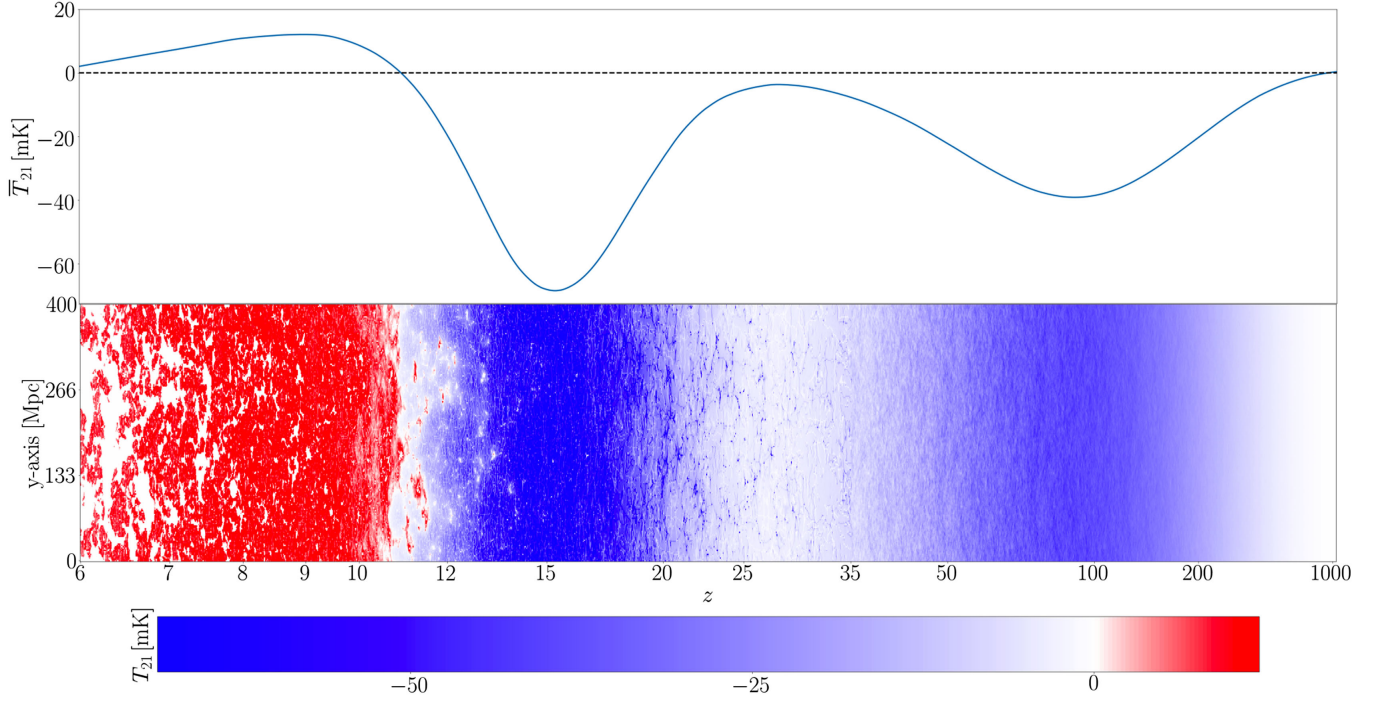


FIG. 2. Top panel: global brightness temperature as a function of redshift. Bottom panel: fluctuations in the brightness temperature as a function of redshift. Here we present the facet of the lightcone box that is generated by 21cmFirstCLASS. For better visualization, the box that was used for this simulation was of size 400 Mpc and contained 200^3 cells. The fluctuation pattern seen here is derived from an approximated scale-independent growth, whereas in principle scale-dependent growth should be considered. This assumption will be relaxed in the next version of 21cmFirstCLASS. See more details on that point in Paper II.

IGM (taking the spin temperature with it) above the CMB temperature, which would lead to an emission feature in the signal. Eventually, stellar radiation reionizes the gas in the IGM and bubbles of ionized hydrogen begin to emerge. After the *reionization* epoch is over, $\tau_{21} \rightarrow 0$, and the 21-cm signal vanishes.

There are three important quantities which govern the brightness temperature during the cosmic dawn and afterward. These are the Ly α flux J_α (since $\tilde{x}_\alpha \propto J_\alpha$), the gas kinetic temperature T_k , and the ionization fraction $x_e \equiv n_e/(n_H + n_{\text{He}})$, where n_e , n_H and n_{He} , are the free-electron, hydrogen-nuclei and helium-nuclei number-densities, respectively. We will not focus on prescriptions for evaluating J_α in this paper and instead refer the reader to Refs. [85,125,128,131] for more details. The evolution of T_k is determined from

$$\frac{dT_k}{dz} = \frac{dt}{dz} \left[-2HT_k + \Gamma_C(T_\gamma - T_k) + \frac{dT_k}{dt} \Big|_{\text{ext}} \right], \quad (3)$$

where $dt/dz = -[H(1+z)]^{-1}$, H is the Hubble parameter, and Γ_C is the Compton heating rate,

$$\Gamma_C \equiv \frac{8\pi^2\sigma_T(k_B T_\gamma)^4}{45\hbar^3 c^4 m_e} \frac{x_e}{1+x_e}. \quad (4)$$

Here, c is the speed of light, \hbar is the (reduced) Planck constant, k_B is Boltzmann's constant, m_e is the electron mass, and σ_T is the Thomson cross section. The term $dT_k/dt|_{\text{ext}}$ that appears in Eq. (3) represents the ‘‘external’’ heating rates,

$$\frac{dT_k}{dt} \Big|_{\text{ext}} = \epsilon_{\text{ext}} + \frac{2}{3} \frac{T_k}{1+\delta_b} \frac{d\delta_b}{dt} - \frac{T_k}{1+x_e} \frac{dx_e}{dt}, \quad (5)$$

where ϵ_{ext} denotes the heating rates that come from external sources, mainly x-ray heating (but Ly α as well as CMB heating rates [83,95,96] can be included), and $\delta_b \equiv \delta\rho_b/\bar{\rho}_b$ is the contrast in the baryon-density fluctuations. The reason why we classify the last two terms in Eq. (5) as ‘‘external’’ heating rates, even though they are sourced by the adiabatic cooling of the IGM, will become clear in Appendixes B and C where we derive the tight coupling approximations.

From Eqs. (3)–(5) it can be seen that the evolution of T_k depends on x_e , especially at early times when the Compton heating rate dominates. The exact detailed evolution of x_e at early times on the other hand is quite intricate as it requires tracking the recombination states of both hydrogen and helium, while taking into account excitations to high-order energy levels. In the seminal work of Refs. [132,133], these effects have been shown to have a subpercent impact on the evolution of x_e , making them crucial for analyzing

the CMB anisotropies at the precision level of the Planck satellite data. A state-of-the-art recombination code that implements these effects and is publicly available is HyRec,³ which we have incorporated in our 21cmFirstCLASS code.

Yet, in order to derive the evolution of temperature and ionization fluctuations within an error of a few percentages, we show in Paper II that it is sufficient to consider Peebles' effective three-level atom model [134], in which the evolution of x_e reads as

$$\frac{dx_e}{dz} = \frac{dt}{dz} \left[\frac{dx_e}{dt} \Big|_{\text{reio}} + \mathcal{C}(\beta_{\text{ion}}(1-x_e) - \alpha_{\text{rec}}n_{\text{H}}x_e^2) \right], \quad (6)$$

where α_{rec} is the recombination rate (in units of cm^3/sec), β_{ion} is the early photoionization rate, and \mathcal{C} is the Peebles coefficient (see Appendix A in Paper II for more details on the Peebles coefficient). The term $dx_e/dt|_{\text{reio}}$ denotes the reionization rate at late times. At early times (long before reionization started), the recombination rate and photoionization rates were in equilibrium, implying that

$$\beta_{\text{ion}} = \alpha_{\text{rec}} \left(\frac{m_e k_B T_\gamma}{2\pi\hbar^2} \right)^{3/2} e^{-\epsilon_0/(k_B T_\gamma)}, \quad (7)$$

where $\epsilon_0 = 13.6$ eV is the ionization energy of the hydrogen atom from its ground state.

Since the standard 21cmFAST code begins its calculations at $z = 35$, the β_{ion} term is completely negligible and was omitted. The recombination rate is the case-A recombination rate which accounts for recombination to the ground state [135]. In addition, the factor \mathcal{C} is not interpreted as the Peebles coefficient but rather as the clumping factor $\langle x_e^2 \rangle / \langle x_e \rangle^2$ [136], which the code sets as a constant with a value of 2 to account for unresolved subgrid fluctuations. This serves as an excellent approximation to the evolution of x_e at late times. We have confirmed with 21cmFirstCLASS that using HyRec at all redshifts almost replicates the same x_e evolution at low redshifts,⁴ while not introducing errors in the 21-cm power spectrum that are larger than HERA's sensitivity (see for example Fig. 3 and further discussion in Sec. IV).

III. INITIAL CONDITIONS

Our code, 21cmFirstCLASS, is composed of two main codes: (1) CLASS, which generates the consistent initial conditions at recombination, and (2) a modification of 21cmFAST, which uses the initial conditions from CLASS to

generate the initial box and then evolves this box until the 21-cm signal vanishes. In the remaining parts of this paper, we use a box of comoving size 256 Mpc and a resolution⁵ of 128^3 cells, and initialize the evolution at recombination. We have confirmed that increasing these specifications does not alter the 21-cm power spectrum beyond HERA's sensitivity.

A. CLASS

In the standard 21cmFAST, the user can vary the cosmological parameters fairly easily from the Python wrapper. The varied parameters however only enter in the C code, while the initial conditions for the simulation remain the same, regardless of the values of the cosmological parameters that were set by the user. This property of 21cmFAST makes it inadequate for studying degeneracies between the cosmological parameters and the astrophysical parameters, especially if physics beyond the standard model is considered (see Sec. VI). In our code, 21cmFirstCLASS, the initial conditions for the simulation are completely consistent with the input set of cosmological parameters.

To get the correct initial conditions we use CLASS. We allow the user to work with either the primordial curvature amplitude A_s (which is commonly used in the CMB and inflation communities), or with the standard 21cmFAST σ_8 parameter, the matter-density variance, smoothed on a sphere of radius $R_8 = 8h^{-1}$ Mpc. Given the current matter-density transfer function $\mathcal{T}_m(k, z=0)$, which is one of the outputs of CLASS, they are related by

$$\sigma_8^2 = A_s \int_0^\infty \frac{dk}{k} \left(\frac{k}{k_\star} \right)^{n_s-1} W^2(kR_8) \mathcal{T}_m^2(k, z=0), \quad (8)$$

where $k_\star = 0.05 \text{ Mpc}^{-1}$ is the CMB pivot scale and $W(kR_8) = 3(kR_8)^{-3} [\sin(kR_8) - kR_8 \cos(kR_8)]$ is the Fourier transform of a top-hat filter of radius R_8 . We note that in ΛCDM simulations we run CLASS with a high $k_{\text{max}} = 4000 \text{ Mpc}^{-1}$, which is necessary to get the correct $\sigma(R)$ at the relevant scales for 21cmFAST. CLASS also computes the background quantities $\bar{T}_k(z)$, and $\bar{x}_e(z)$, the latter via HyRec.⁶ We then define the moment of recombination, and the starting point of our simulation, to be the redshift that solves $x_e(z_{\text{rec}}) \equiv 0.1$. For the fiducial set of cosmological parameters we use, it is $z_{\text{rec}} \approx 1069$.

In addition, we also evaluate $\mathcal{T}_{v_{\text{cb}}}(k, z_{\text{rec}})$, the transfer function of V_{cb} during recombination, with

³<https://github.com/nanoomlee/HYREC-2>.

⁴The incorporation of HyRec was done only at the code section of 21cmFAST that evolves x_e , while leaving the reionization code unchanged. Therefore, the reionization history remains almost the same in 21cmFAST and 21cmFirstCLASS—see more in Sec. IV.

⁵To be perfectly clear, by 128 we refer to the parameter HII_DIM, and not the parameter DIM, which is 3 times larger.

⁶Care has to be taken when converting from CLASS conventions for x_e , which is n_e/n_{H} , to 21cmFAST conventions, for which $x_e \equiv n_e/(n_{\text{H}} + n_{\text{He}})$.

$$T_{v_{cb}}(k, z_{\text{rec}}) = \left| \frac{\theta_c(k, z_{\text{rec}}) - \theta_b(k, z_{\text{rec}})}{kc} \right|, \quad (9)$$

where θ_c (θ_b) is the Fourier transform of the divergence of the CDM (baryons) velocity, quantities that are also given by CLASS. We construct interpolation tables for $T_m(k, z=0)$, $T_{v_{cb}}(k, z_{\text{rec}})$, $\bar{T}_k(z)$ and $\bar{x}_e(z)$, and they are then used to replace the default tables used by 21cmFAST.

Finally,⁷ we also save CLASS’s scale-independent growth factor $D(z)$ in a new interpolation table that goes into 21cmFAST. This quantity is obtained in CLASS by solving a second order differential equation. To avoid solving this equation for $D(z)$, in the standard 21cmFAST the “Dicke growth” factor is used [137,138]. This is an analytical fit to the growth factor that works particularly well below $z = 35$. However, this fit underestimates the true growth factor at $z \gtrsim 100$, and that can lead to an error of a few percentages in the fluctuation pattern of T_k and x_e at low redshifts. Moreover, these errors can propagate to the global signal at $10 \lesssim z \lesssim 20$, when nonlinearities become important. To avoid introducing errors in the calculation, without sacrificing run-time or computational cost, we adopt CLASS’s growth factor in 21cmFirstCLASS. For more details on the scale-independent growth factor and its effect on the 21-cm signal, see Appendix A.

B. 21cmFAST

The initial density and velocity boxes in 21cmFirstCLASS are generated in a similar manner as in the standard 21cmFAST. Prior to $z = 35$, we evolve the matter-density fluctuations linearly,⁸ though we have confirmed that evolving the density box nonlinearly at high redshifts yields the same 21-cm power spectrum at low redshifts. As for the initial $T_k(z_{\text{rec}})$ and $x_e(z_{\text{rec}})$ boxes, we assume that they are homogeneous. As we discuss in Paper II, an homogeneous $T_k(z_{\text{rec}})$ box is an excellent assumption, much more than the homogeneous $T_k(z = 35)$ box that is assumed in the standard 21cmFAST. For the x_e box, the assumption of homogeneity at $z_{\text{rec}} \approx 1069$ is not justified (though it is still better than assuming homogeneity at

⁷We also adopt from CLASS the helium mass-fraction Y_{He} as well as the mean of the relative velocity between CDM and baryons during recombination $\langle V_{cb}(z_{\text{rec}}) \rangle$. In addition, our code also has the ability to compute the fitting parameters A_p , k_p and σ_p on the fly [see more details in Eq. (14) of Ref. [86]], though we find that their effect on the brightness temperature is negligible compared to the effect that V_{cb} has on the minimum halo mass that can still host stars—see Sec. VID.

⁸In this paper we assume $\delta_b(z) = D(z)\delta_b(z=0)$. We comment that although such a scale-independent growth of δ_b is inadequate at high redshifts, our conclusions in this paper are not affected by this crude assumption, which shall be relaxed in the version of 21cmFirstCLASS that will soon be made public. We elaborate much more on this subtlety in Paper II.

$z = 35$), but we show in Paper II that the resulting 21-cm power spectrum is not very sensitive to this assumption. Ideally, one could use the T_k and x_e transfer functions from CLASS to draw the initial boxes, as was done in Ref. [105]. In Λ CDM, such an approach would remove the necessity of starting the simulation at recombination, since all the fluctuations prior to $z = 35$ are linear to a very good approximation. Yet, we stress that this approach is no longer valid in some beyond Λ CDM cosmologies (like the one we discuss in Sec. VI) where nonlinearities have an important role even before $z = 35$.

We then solve numerically the differential equation for T_k [Eq. (3)] at each cell, using the Euler method, to promote T_k to the next redshift step, as in the standard 21cmFAST. The difference, though, is the step size. In 21cmFAST, a logarithmic redshift sampling is used such that $(1 + z_n)/(1 + z_{n+1}) = 1.02$, where z_n is the n th redshift sample in the simulation, such that the step size $\Delta z_n = z_n - z_{n+1}$ is ~ 0.1 at $z = 6$ and ~ 0.6 at $z = 35$. This redshift sampling scheme is insufficient at higher redshifts, and we therefore work with a constant step size of $\Delta z_n = 0.1$ at $35 \leq z \leq 980$. Above $z = 980$ this step size is also not enough, and we have to switch to $\Delta z_n = 0.01$ to simulate the evolution precisely. This fine redshift sampling above $z = 980$ comes with a price; although no computationally expensive astrophysical calculations are required, the many redshift samples extend the run-time of the code considerably. Yet, there is a much more clever way to evolve T_k above $z = 980$ with excellent precision, without generating so many redshift samples. Briefly, the idea is to treat the baryons and the CMB as a single fluid when the conditions for the *Compton-tight coupling approximation (TCA)* are satisfied. We provide more details on that method in Appendix B.

The normal evolution of x_e in 21cmFirstCLASS is done with HyRec, though our code can be configured to solve instead the Peebles model, Eq. (6), with the recombination rate $\alpha_{\text{rec}} = \alpha_B$ of RECFast [139,140], where α_B is the case-B recombination rate (which accounts for recombination only to the first excited state). As in CLASS, we use the default “SWIFT” model of HyRec when $T_k/T_\gamma < 0.1$, and otherwise we use its “PEEBLES” model, which is quite similar to Eq. (6) above. In CLASS, however, two quantities are solved with HyRec; these are x_{H} and x_{He} . Their relation to x_e is $x_e = x_{\text{H}} + (n_{\text{He}}/n_{\text{H}})x_{\text{He}}$. From this equation the physical meaning of x_{H} (x_{He}) should be clear—it is the contribution of the ionized hydrogen (helium) number density to the total free-electron number density. In 21cmFirstCLASS we assume $x_e \approx x_{\text{H}}$, which is justified because (1) helium recombination is over long before hydrogen recombination begins, at $z \sim 1500$; (2) the freeze-out value of x_{He} is an order of magnitude smaller than the freeze-out value of x_{H} ; and (3) the contribution of x_{He} to x_e is suppressed by the factor $n_{\text{He}}/n_{\text{H}} \approx 0.08$. As can be seen in Fig. 3, the assumption $x_e \approx x_{\text{H}}$ is indeed an excellent approximation.

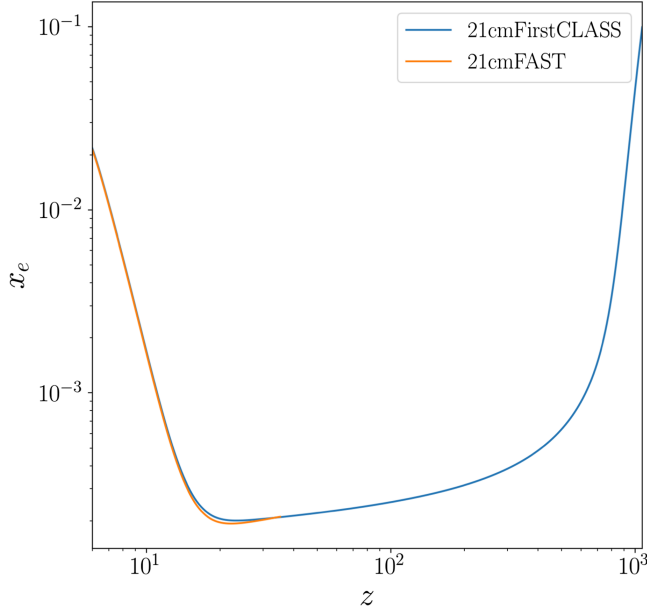


FIG. 3. Comparison of the global x_e evolution between 21cmFirstCLASS and 21cmFAST (in both cases we use CLASS to obtain the correct initial conditions). In the former, HyRec is used all the way from recombination to $z = 6$. In the latter, the simulation begins at $z = 35$, and x_e is evolved differently (see more details at the end of Sec. II). Note the consistency at $z = 35$ (though early ionization fluctuations slightly change the mean of the box in 21cmFirstCLASS—see more details in Paper II).

IV. COMPARING 21cmFirstCLASS WITH 21cmFAST

In Λ CDM, all fluctuations at the relevant scales prior to $z = 35$ can be considered linear to a very good approximation. Consistency therefore implies that 21cmFirstCLASS must be able to generate the same initial conditions as in 21cmFAST, at $z = 35$. Such a sanity check is demonstrated in Fig. 3, where we present the evolution of \bar{x}_e in the two codes. At $z = 35$ the two codes agree. Afterward, the solution of the two codes deviates because of the different evolution, as was outlined at the end of Sec. II. This leads to a maximum 5% difference.

Yet, this error does not propagate to the observable—the brightness temperature—as can be seen in Fig. 4. This is because τ_{21} is not proportional to x_e but rather to x_{HI} , the neutral hydrogen fraction. Before the onset of reionization, we can approximate $x_{\text{HI}} \approx 1 - x_e$, and a simple calculation shows that the 5% difference in \bar{x}_e translates to merely a 0.001% error in \bar{x}_{HI} .

Even though the first-order statistics of the box, namely its mean, is consistent in both codes, it does not imply that higher-order statistics, like the two-point function, are the same. The Fourier transform of the two-point correlation function is the power spectrum. For the 21-cm signal, it is customary to work with a power spectrum that has units of mK^2 ,

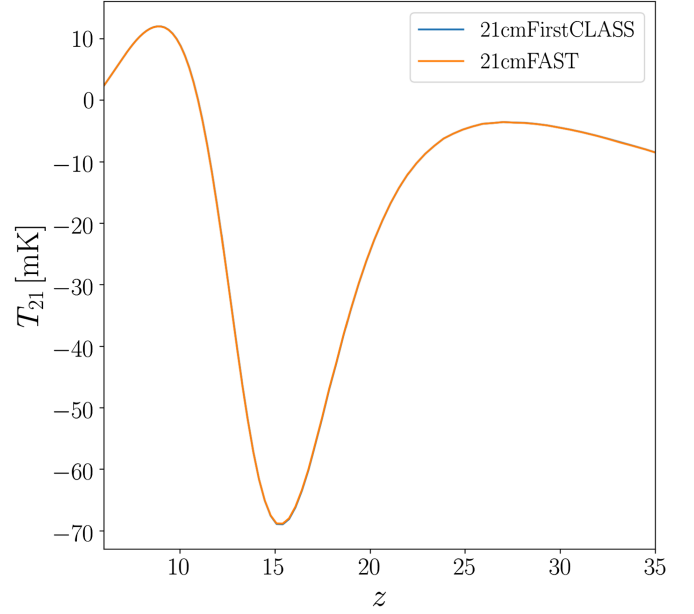


FIG. 4. Comparison of the global brightness temperature between 21cmFirstCLASS and 21cmFAST. The curves almost totally overlap.

$$\Delta_{21}^2(k, z) = \frac{k^3 \bar{T}_{21}^2(z) P_{21}(k, z)}{2\pi^2}, \quad (10)$$

where \bar{T}_{21} is the global brightness temperature and $P_{21}(k, z)$ is the angle-averaged Fourier transform of the two-point function $\langle \delta_{21}(\mathbf{x}, z) \delta_{21}(\mathbf{x}', z) \rangle$, while δ_{21} is the local contrast in the brightness temperature, $\delta_{21}(\mathbf{x}, z) \equiv T_{21}(\mathbf{x}, z) / \bar{T}_{21}(z) - 1$. We use the POWERBOX⁹ package [141] to compute $\Delta_{21}^2(k, z)$ from chunks of the light cone box of 21cmFirstCLASS.

In Fig. 5, we compare the 21-cm power spectrum of 21cmFirstCLASS and 21cmFAST. Unlike the global signal, clear differences can be seen—only because we started the simulation at a different initial time (recombination in 21cmFirstCLASS and $z = 35$ in 21cmFAST). The origin of this effect comes from *early temperature and ionization fluctuations*. The impact of the former kind of fluctuations—temperature fluctuations—on the 21-cm power spectrum was first discussed in Ref. [81]. In Paper II we extend the discussion on early fluctuations and explore in great detail the contribution of both temperature and ionization fluctuations. Still, Fig. 5 suggests that taking into account early temperature and ionization fluctuations results in a maximum distortion of $\sim 20\%$ to the 21-cm power spectrum at $k = 0.3 \text{ Mpc}^{-1}$, $z = 17$, which is below HERA's noise level. We note that this is in slight contrast with the conclusions of Ref. [81], where larger deviations are

⁹<https://github.com/steven-murray/powerbox>.

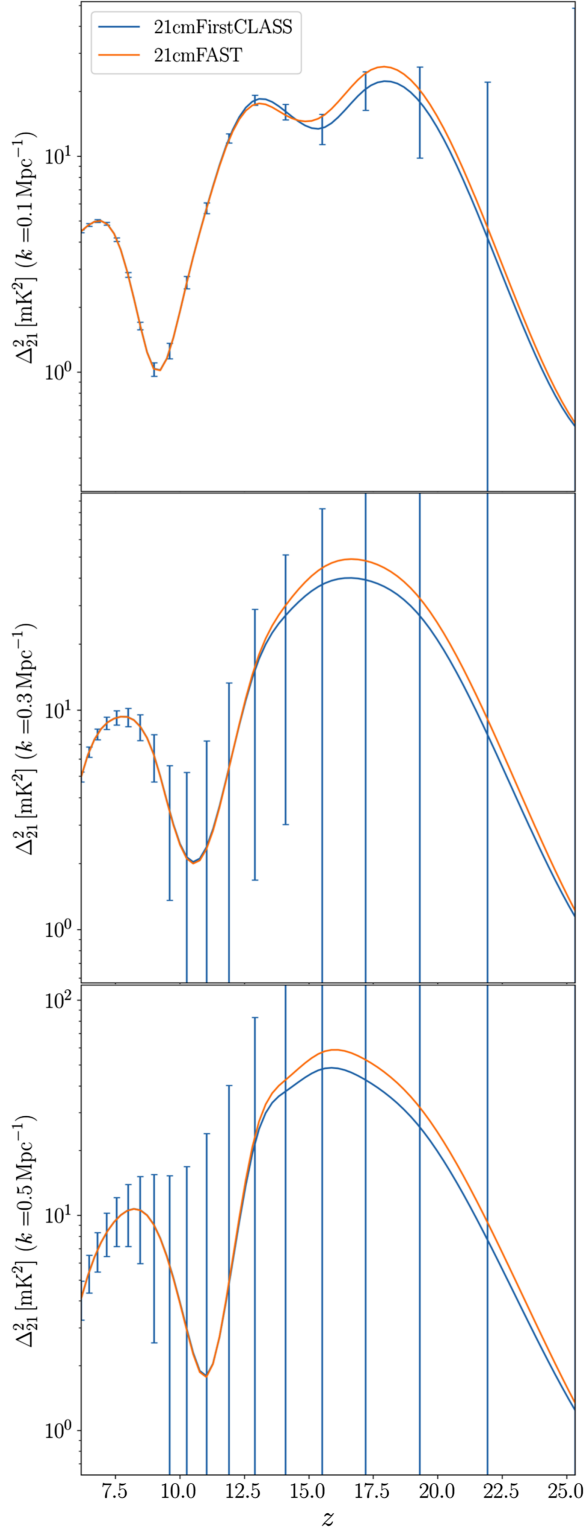


FIG. 5. Comparison of the 21-cm power spectrum between 21cmFirstCLASS and 21cmFAST, for three different wave numbers. The error bars correspond to HERA’s noise in its design sensitivity under the assumption of optimistic foregrounds (see Sec. V). As we explain in the text, the source for the differences between the curves is early temperature and ionization fluctuations—see more details in Paper II.

claimed. Again, we refer the reader to Paper II for an elaborate discussion on that point.

V. COMBINING 21cm AND CMB DATA

The anisotropies in the CMB have been proven to be an invaluable source for studying different cosmological models. Likewise, the global 21-cm signal and its inhomogeneities are expected to contain rich information that can be employed in cosmological studies of Λ CDM and beyond. Because 21cmFirstCLASS already calculates the CMB anisotropies via CLASS, it is only natural to include them as part of our analysis. These two observables are uncorrelated and thus can be used to break degeneracies in the other observable. We will demonstrate this point below while working with the Fisher formalism.

A. Fisher formalism

In the Fisher formalism, the covariance matrix is given by the inverse of the Fisher matrix [142,143],

$$F_{\alpha,\beta}^{21\text{cm}} = \sum_{k,z} \frac{\partial \Delta_{21}^2(k,z)}{\partial \alpha} \frac{\partial \Delta_{21}^2(k,z)}{\partial \beta} \frac{1}{[\delta \Delta_{21}^2(k,z)]^2}. \quad (11)$$

Here, α and β denote the free parameters that we vary. We vary both cosmological parameters and astrophysical parameters¹⁰ [144],

$$(\alpha, \beta) \in \left\{ h, \Omega_m, \Omega_b, A_s, L_X^{(\text{II})}, f_*^{(\text{II})}, f_{\text{esc}}^{(\text{II})}, A_{\text{LW}}, A_{v_{cb}}, T_{\text{vir}}^{(\text{II})} \right\}. \quad (12)$$

The varied astrophysical parameters in our analysis are displayed in the second row. $L_X^{(\text{II})}$ is the x-ray luminosity (normalized by the star formation rate, in units of $\text{erg sec}^{-1} M_\odot^{-1} \text{ year}$), $f_*^{(\text{II})}$ is the star formation efficiency, $f_{\text{esc}}^{(\text{II})}$ is the escape fraction of ionizing photons, A_{LW} ($A_{v_{cb}}$) characterizes the amplitude of the LW (V_{cb}) feedback on $M_{\text{mol,min}}$, and $T_{\text{vir}}^{(\text{II})}$ is the minimum halo virial temperature. Quantities with a superscript (II) correspond to pop-II stars. We also vary the analogous pop-III parameters, around the same fiducial values as the pop-II ones.

The parameters listed in Eq. (12) are not the only parameters that control the 21-cm signal and the CMB. There are many more astrophysical parameters, like the mean-free path of photons through ionized regions, yet for

¹⁰Although some of the astrophysical parameters in 21cmFAST are defined logarithmically (e.g. $L_X^{(\text{II})} = 40.5$), in our analysis we make sure we vary the linear parameters (e.g. $L_X^{(\text{II})} = 10^{40.5}$). In Fig. 6, when we present the confidence level ellipses of $\log_{10} L_X$, we apply the appropriate Jacobian transformation.

our purposes of demonstrating the joint analysis of 21-cm and CMB, the astrophysical parameters in Eq. (12) suffice. Another subtlety in our analysis is that we fix τ_{re} , although its value can be inferred from the reionization model [145]. A consistent treatment to incorporate τ_{re} in 21cmFirstCLASS would require computing it from the output of 21cmFAST and feeding its value to CLASS. We leave this kind of analysis for future work.

The quantity $\delta\Delta_{21}^2(k, z)$ that appears in the denominator of Eq. (11) denotes the noise of the experiment, in our case, HERA. We simulate HERA's design sensitivity noise with 21cmSense¹¹ [146,147]. In its final stage, HERA will have in its core 331 antennas, each of which has a diameter of 14 m, arranged in a hexagonal array with 11 antennas at its base. We assume the frequency range of HERA will span between 50 MHz ($z = 27.4$) and 225 MHz ($z = 5.3$) with a bandwidth of 8 MHz. This gives a total number of 22 different frequency bands, but in our analysis, to be conservative, we discard the bands below $z = 6$ as in that regime the exact reionization details are highly uncertain, leaving us with 19 redshift bins in total. In each frequency band we assume there are 82 channels, corresponding to 1024 channels over 100 MHz bandwidth [64]. In addition, we assume HERA operates for six hours per night during 540 days in total, the receiver temperature is $T_{\text{rec}} = 100$ K and the sky temperature follows $T_{\text{sky}}(\nu) = 60 \text{ K}(\nu/300 \text{ MHz})^{-2.55}$.

Finally, we consider in our analysis ‘‘pessimistic,’’ ‘‘moderate,’’ and ‘‘optimistic’’ foreground scenarios. In the moderate (pessimistic) foreground scenario, the wedge¹² is assumed to extend to $\Delta k_{\parallel} = 0.1h \text{ Mpc}^{-1}$ beyond the horizon wedge limit, and all baselines are added coherently (incoherently), while in the optimistic foreground scenario the boundary of the foreground wedge is set by the FWHM of the primary beam of HERA, and there is no contamination beyond this boundary.

As motivated above, to break degeneracies in the 21-cm signal, we consider future measurements from CMB-S4 [150]. We follow Refs. [145,151–153] and evaluate the Fisher matrix associated with CMB-S4 measurements via

$$F_{\alpha\beta}^{\text{CMB}} = \sum_{\ell=30}^{3000} \frac{2\ell+1}{2} f_{\text{sky}} \text{Tr} \left[C_{\ell}^{-1} \frac{\partial C_{\ell}}{\partial \alpha} C_{\ell}^{-1} \frac{\partial C_{\ell}}{\partial \beta} \right], \quad (13)$$

where $f_{\text{sky}} = 40\%$ is the sky-fraction coverage and the matrices $C_{\ell}(\nu)$ are (neglecting the lensing contribution)

$$C_{\ell}(\nu) = \begin{bmatrix} \tilde{C}_{\ell}^{\text{TT}}(\nu) & C_{\ell}^{\text{TE}}(\nu) \\ C_{\ell}^{\text{TE}}(\nu) & \tilde{C}_{\ell}^{\text{EE}}(\nu) \end{bmatrix}. \quad (14)$$

Here, tilde-less quantities are the noise-free CMB anisotropies power spectrum that we take from CLASS, while tilde-full quantities include the CMB-S4 noise contribution, $\tilde{C}_{\ell}^{\text{XX}} = C_{\ell}^{\text{XX}} + N_{\ell}^{\text{XX}}$. The noise power spectra are given by

$$N_{\ell}^{\text{TT}}(\nu) = \Delta_T^2(\nu) e^{\ell(\ell+1)\sigma_b^2(\nu)}, \quad N_{\ell}^{\text{EE}}(\nu) = 2 \times N_{\ell}^{\text{TT}}(\nu), \quad (15)$$

where $\Delta_T(\nu)$ is the temperature sensitivity and $\sigma_b(\nu) = \theta_{\text{FWHM}}(\nu)/\sqrt{8 \ln 2}$, with the full-width-half-maximum θ_{FWHM} given in radians. We consider a single frequency channel, centered at $\nu = 145$, GHz with $\Delta_T = 1.5 \mu\text{K} \cdot \text{arcmin}$ and $\theta_{\text{FWHM}} = 1.4 \text{ arcmin}$. Finally, we add the HERA and CMB-S4 Fisher matrices,

$$F_{\alpha\beta}^{\text{tot}} = F_{\alpha\beta}^{21\text{cm}} + F_{\alpha\beta}^{\text{CMB}}. \quad (16)$$

B. Forecasts

Armed with our Fisher formalism, we now vary the free parameters of Eq. (12), while imposing Planck 2018 priors [40] on the cosmological parameters. In our analysis, we only impose priors on h, Ω_m, Ω_b and A_s . Figure 6 shows our results. As expected, adding the CMB-S4 information helps in mitigating all the degeneracies between the different parameters, especially in the cosmological parameters. Because the CMB anisotropies depend only on the cosmological parameters, and the cosmological parameters are not strongly degenerate with the free astrophysical parameters in our analysis, including the information of the CMB power spectra does not help considerably in alleviating degeneracies in the astrophysical parameters. Unlike the cosmological parameters, the well-known degeneracy between $f_*^{(\text{II})}$ and $f_{\text{esc}}^{(\text{II})}$ is evident [143,154,155]. These parameters exhibit a negative correlation as the ionization efficiency is proportional to the product of $f_*^{(\text{II})}$ and $f_{\text{esc}}^{(\text{II})}$. Similarly, as the x-ray heating efficiency is proportional to the product of $f_*^{(\text{II})}$ and $L_X^{(\text{II})}$, there is a negative correlation between these parameters as well. Note that the degeneracy of $f_{\text{esc}}^{(\text{II})}$ and $L_X^{(\text{II})}$ with $f_*^{(\text{II})}$ is not complete because the latter also determines the efficiency of the Ly α flux.

Not unexpectedly, for ΛCDM , CMB-S4 will have more constraining power than HERA, as indicated by Fig. 7. Here, all the astrophysical parameters were marginalized (fixed) when only the information of HERA (CMB-S4) was considered. As we shall see in the next section, this statement can be different for beyond ΛCDM cosmologies, and the 21-cm data can play a more dominant role.

¹¹<https://github.com/rasg-affiliates/21cmSense>.

¹²Our analysis here follows the HERA approach of using only data outside the foreground ‘‘wedge’’ [148,149], thus effectively avoiding foregrounds instead of trying to remove them from the data.

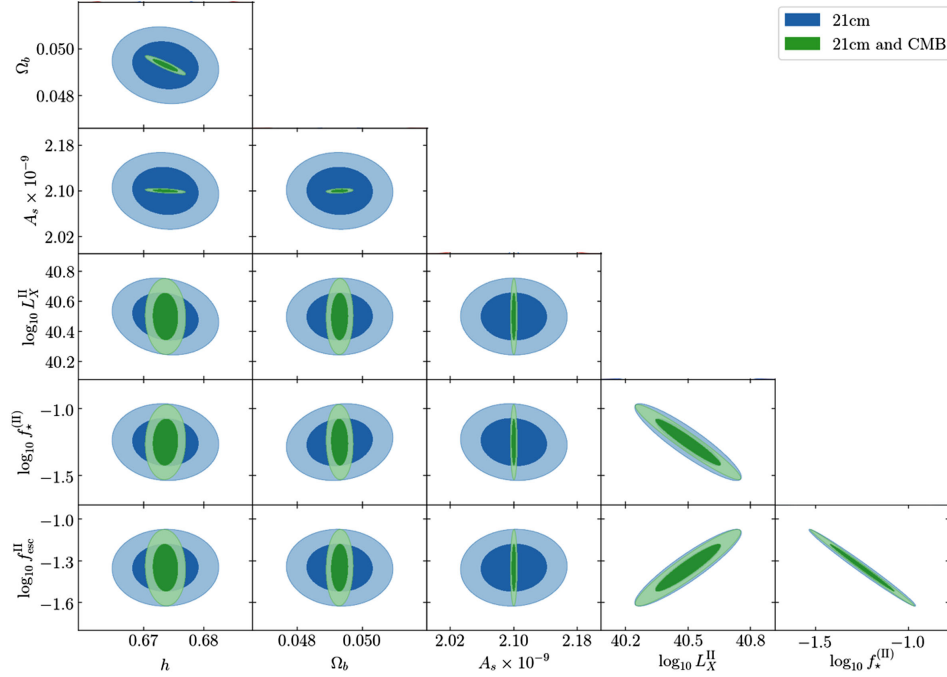


FIG. 6. Forecasts of 1- σ and 2- σ confidence levels of some of the free parameters in Eq. (12) (the rest of the parameters not shown here have been marginalized), while imposing Planck 2018 priors [40] on the cosmological parameters. Blue ellipses correspond to HERA-only forecasts, while the green ellipses account for information coming from CMB-S4 as well. Results are shown for the moderate foreground scenario, although they barely change when a pessimistic foreground scenario is considered.

VI. SCATTERING DARK MATTER

To demonstrate the potential of 21cmFirstCLASS in studying nonlinear models beyond the standard model, we now consider SDM. In this model, a fraction f_χ of the dark matter consists of particles of mass m_χ that interact directly in a nongravitational manner with baryons. In this paper, we focus on $f_\chi = 100\%$ and $m_\chi = 1$ MeV, although these parameters can be varied in our code (we vary them in future work). The cross section for the baryons-SDM interaction is parametrized by $\sigma = \sigma_n(v/c)^n$, where v is the relative velocity between the interacting baryon and SDM particles. We also fix $n = -4$ to correspond to a Coulomb-type interaction (we will relax this assumption in future work), and thus σ_{-4} is the only free parameter in the model we are considering.

There are two consequences to the direct interaction between the baryons and the SDM: (1) they transfer energy, whereby the cold SDM is able to cool the hotter baryonic gas, while the baryons heat the SDM and increase its temperature T_χ , and (2) the bulk relative velocity $V_{\chi b}$ between the two fluids is decreased via a drag force that they apply on each other. The former effect made the SDM a very popular dark matter candidate after the EDGES Collaboration announced they measured a minimum value of $\bar{T}_{21} = -500_{-500}^{+200}$ mK (at 99% confidence level) [156], which is 3.8σ below Λ CDM expectation. More recent results from the SARAS-3 experiment [157] do not reproduce the detection, however.

A. Evolution equations

Below we write the differential equations that have to be solved in the SDM model. These equations were originally derived in Ref. [100] and appeared since then in many works in the literature. We use a slightly different notation which will be useful for the derivation of the *DM-TCA* equations (see Appendix C). The SDM interaction modifies the evolution equation for T_k , Eq. (3), which now reads as (note that from this point on we will mostly denote the gas temperature with T_b in order to have symmetrical expressions for the baryons and SDM)

$$\frac{dT_b}{dz} = \frac{dt}{dz} \left[-2HT_b + \Gamma_C(T_\gamma - T_b) + \frac{2\dot{Q}_b}{3k_B} + \frac{dT_b}{dt} \Big|_{\text{ext}} \right], \quad (17)$$

and a similar equation for the SDM temperature exists,

$$\frac{dT_\chi}{dz} = \frac{dt}{dz} \left[-2HT_\chi + \frac{2\dot{Q}_\chi}{3k_B} + \frac{dT_\chi}{dt} \Big|_{\text{ext}} \right], \quad (18)$$

where

$$\frac{dT_\chi}{dt} \Big|_{\text{ext}} = \frac{2}{3} \frac{T_\chi}{1 + \delta_\chi} \frac{d\delta_\chi}{dt}, \quad (19)$$

and $\delta_\chi \equiv \delta\rho_\chi/\bar{\rho}_\chi$ is the SDM density contrast. To solve for T_b and T_χ , we need a third differential equation, for

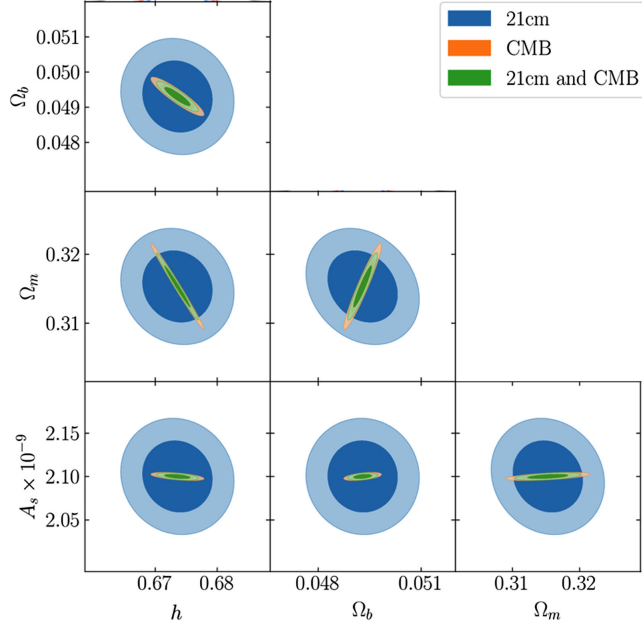


FIG. 7. Forecasts of 1- σ and 2- σ confidence levels of the free cosmological parameters in Eq. (12), while imposing Planck 2018 priors [40] on the cosmological parameters. Blue (orange) ellipses correspond to forecasts when only information from HERA (CMB-S4) is considered, while the green ellipses account for information coming from both HERA and CMB-S4. All the astrophysical parameters have been marginalized (fixed) in the calculation of the HERA (CMB-S4) Fisher matrix. For HERA, results are shown for the moderate foreground scenario, although they barely change when the pessimistic foreground scenario is considered.

the evolution of the bulk relative velocity between the fluids $V_{\chi b}$,

$$\begin{aligned} \frac{dV_{\chi b}}{dz} &= \frac{dt}{dz} [-HV_{\chi b} - D(V_{\chi b})] \\ &= \frac{dt}{dz} \left[-HV_{\chi b} - \sum_t D_t(V_{\chi b}) \right], \end{aligned} \quad (20)$$

where $D(V_{\chi b})$ is the mutual drag force that acts on the baryons and SDM fluids. It is the sum of all the drag forces that arise from the interaction of an SDM particle with a standard model target particle of type t ,

$$D_t(V_{\chi b}) = \frac{\rho_{\text{tot}} \sigma_{-4} c^4}{\rho_b u_{\chi t}^2} \frac{\rho_t F(r_t)}{m_t + m_\chi}. \quad (21)$$

Here, ρ_b ($\rho_\chi = f_\chi \rho_c$) is the baryon (SDM) energy density, $\rho_{\text{tot}} = \rho_b + \rho_\chi$ (it is not the total matter energy density if $f_\chi < 1$), m_t is the mass of the target particle, and ρ_t is the energy density of the target particles. The function $F(r_t)$ is

$$F(r_t) = r_t^{-2} \left[\text{erf} \left(\frac{r_t}{\sqrt{2}} \right) - \sqrt{\frac{2}{\pi}} r_t e^{-r_t^2/2} \right] \Big|_{r_t \ll 1} \approx \sqrt{\frac{2}{9\pi}} r_t, \quad (22)$$

where $r_t \equiv V_{\chi b}/u_{\chi t}$ and $u_{\chi t}$ is the thermal velocity,

$$u_{\chi t} \equiv \sqrt{\frac{k_B T_b}{m_t} + \frac{k_B T_\chi}{m_\chi}}. \quad (23)$$

The cooling/heating rates \dot{Q}_b and \dot{Q}_χ that appear in Eqs. (17) and (18) are given by

$$\dot{Q}_b = \frac{3}{2} \Gamma_{\chi b} k_B (T_\chi - T_b) + \frac{\rho_\chi}{\rho_{\text{tot}}} V_{\chi b} \sum_t \frac{m_\chi m_b}{m_\chi + m_t} D_t(V_{\chi b}) \quad (24)$$

$$\dot{Q}_\chi = \frac{3 n_b}{2 n_\chi} \Gamma_{\chi b} k_B (T_b - T_\chi) + \frac{\rho_b}{\rho_{\text{tot}}} V_{\chi b} \sum_t \frac{m_\chi m_t}{m_\chi + m_t} D_t(V_{\chi b}), \quad (25)$$

where $n_b = \rho_b/m_b$ ($n_\chi = \rho_\chi/m_\chi$) is the baryon (SDM) number density. Finally, the energy transfer rate $\Gamma_{\chi b}$ is

$$\Gamma_{\chi b} = \sqrt{\frac{2}{\pi}} \frac{2 \sigma_{-4} c^4 \rho_\chi}{3 n_b} \sum_t \frac{\rho_t e^{-r_t^2/2}}{(m_t + m_\chi)^2 u_{\chi t}^3}. \quad (26)$$

Two SDM models are typically considered in the literature.¹³ The first one considers millicharged DM [107–115], in which the target particles are *free* electrons and protons, $n_{t1} = n_{t2} = n_e$, $m_{t1} = m_e$, $m_{t2} = m_p$. Because the number density of the target particles is proportional to x_e , which is very small between recombination and reionization, this model does not generate strong signatures in the 21-cm signal, unless very large cross sections (that are already ruled out by CMB measurements) are considered. Instead, we focus on a baryophilic SDM [99–107], in which SDM interacts with *all* standard model particles, i.e. $\rho_t = \rho_b$ and $m_t = m_b$, where the mean baryon mass is given by

$$m_b = \frac{m_H}{[1 - (1 - m_H/m_{\text{He}}) Y_{\text{He}}](1 - x_e)}, \quad (27)$$

with m_H (m_{He}) the mass of the hydrogen (helium) atom and $Y_{\text{He}} = \rho_{\text{He}}/\rho_b \approx 0.245$ the helium mass fraction.

As in Λ CDM, we solve Eqs. (17)–(20) at each cell using the Euler method, with a step size of $\Delta z_n = 0.1$. At low temperatures, the logarithmic redshift sampling of the standard 21cmFAST below $z = 35$ is not enough, and we continue to work with $\Delta z_n = 0.1$ at the low redshift regime. Furthermore, we note that attempting to solve

¹³There are also models in which the SDM interacts with either protons or electrons, but not both [116–122], and there are models in which the SDM directly interacts with CDM [123,124].

Eqs. (17)–(20) via the Euler method for large cross sections results in overshooting of the solution due to the strong coupling between the baryons and the SDM at low redshifts. We therefore had to devise a dedicated method for solving the equations in the strong coupling limit—this is the *DM-TCA* (in contrast with *Compton-TCA*). We elaborate more on that method in Appendix C.

B. Initial conditions

To generate the SDM initial conditions for 21cmFAST we use a modified version of CLASS¹⁴ in which the SDM fluid variables δ_χ , θ_χ , T_χ are solved simultaneously with the rest of the standard fluid variables of the baryons and CDM (more details on that version can be found in Ref. [101]). The present total matter density transfer function is then given by $\Omega_m \mathcal{T}_m = \Omega_c [(1 - f_\chi) \mathcal{T}_c + f_\chi \mathcal{T}_\chi] + \Omega_b \mathcal{T}_b$. There is a subtlety in the calculation of $\mathcal{T}_m(k, z = 0)$ that we would like to address. The evolution of δ_b and δ_χ depends on the gas temperature T_b since the momentum exchange rate depends on the thermal velocity $u_{\chi t}$. Even though CLASS uses a toy model for the x-ray heating rate ϵ_χ [see Eq. (5)], the resulting transfer function is still correct. The reason for this is that $u_{\chi t}$ competes with $V_{\chi b}$ in the evolution equations of δ_b and δ_χ , and since $V_{\chi b}$ becomes very small already at high redshifts (cf. Fig. 8), $u_{\chi t}$ turns out to have minimal impact on the low-redshift evolution.

We also extract from CLASS the quantity $\mathcal{T}_{v_{\chi b}}(z_{\text{rec}}, k)$, the transfer function of the relative velocity between baryons and SDM at recombination, with an equation similar to Eq. (9). In 21cmFirstCLASS, we then generate a $\mathbf{V}_{\chi b}(\mathbf{k}, z_{\text{rec}})$ box in Fourier space via [158]

$$\mathbf{V}_{\chi b}(\mathbf{k}, z_{\text{rec}}) = i \frac{\mathbf{k}c}{k} \frac{\mathcal{T}_{v_{\chi b}}(k, z_{\text{rec}})}{\mathcal{T}_m(k, z = 0)} \delta_m(\mathbf{k}, z = 0). \quad (28)$$

This yields a $\mathbf{V}_{\chi b}(\mathbf{k}, z_{\text{rec}})$ field that is curlfree and completely correlated with $\delta_m(\mathbf{k}, z = 0)$. In real space, the box of $V_{\chi b}(\mathbf{x}, z_{\text{rec}}) = [\mathbf{V}_{\chi b}(\mathbf{x}, z_{\text{rec}}) \cdot \mathbf{V}_{\chi b}(\mathbf{x}, z_{\text{rec}})]^{1/2}$ has a Maxwell-Boltzmann distribution with an rms of

$$\langle V_{\chi b}^2(z_{\text{rec}}) \rangle = A_s \int_{k_{\text{min}}}^{k_{\text{max}}} \frac{dk}{k} \left(\frac{k}{k_\star} \right)^{n_s - 1} \mathcal{T}_{v_{\chi b}}^2(k, z_{\text{rec}}), \quad (29)$$

where k_{min} (k_{max}) are determined from the box (cell) size.

Two notes must be made on the above prescription. First, the mean of the $V_{\chi b}(\mathbf{x}, z_{\text{rec}})$ box is $\langle V_{\chi b}(z_{\text{rec}}) \rangle = \sqrt{8/(3\pi)} \langle V_{\chi b}^2(z_{\text{rec}}) \rangle^{1/2} \approx 0.92 \langle V_{\chi b}^2(z_{\text{rec}}) \rangle^{1/2}$. Because of the finite box and cell size this is *not* the true globally averaged value of $V_{\chi b}$ at recombination. For example, in Fig. 8 the initial value of $V_{\chi b}$ in all curves is off by $\sim 3\%$. As a consequence, when we plot the mean values of our box at

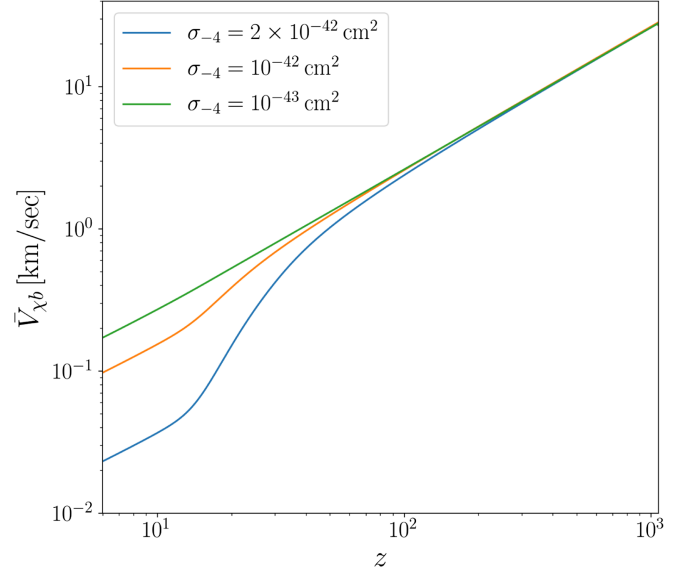


FIG. 8. Evolution of the “global” $V_{\chi b}$ [see caveat below Eq. (29)] for three different cross sections. In this figure and in the upcoming figures we fix $m_\chi = 1$ MeV and $f_\chi = 100\%$.

Sec. VI E, they do not correspond precisely to the true global values. Since in this paper we are mostly interested in the fluctuations of the 21-cm signal, we are not bothered by that nuance. Secondly, the Maxwellianity of $V_{\chi b}$ breaks right after recombination. This is because of the drag term in Eq. (20), as it renders the differential equation for $V_{\chi b}$ nonlinear. Of course, there is no reason to expect that precisely at recombination $V_{\chi b}$ was Maxwellian. In fact, in the derivation of Eqs. (17)–(20), Maxwellianity was assumed throughout. We are therefore being conservative and solve in this work the same equations commonly found in the general SDM literature, despite the inherent inconsistency that this model has. Clearly, the Maxwellianity assumption has to be relaxed, and we leave the study of non-Maxwellianities for future work (see, however, very interesting insights from Refs. [159,160] on that particular subject).

C. Small temperature corrections

The direct coupling between SDM and baryons may cause the temperature of the latter to reach very low values, much less than 1 K (cf. Fig. 9). This requires modifying some of the key quantities used in 21cmFAST.

We take the small temperature correction for the brightness temperature from Ref. [124],

$$T_{21} = \frac{1}{1+z} \left[\frac{\zeta(z)}{e^{\zeta(z)} - 1} T_s - T_\gamma \right] (1 - e^{-\tau_{21}}), \quad (30)$$

where $\zeta(z) = T_\star/T_s(z)$ and $T_\star = 68.2$ mK is the hydrogen hyperfine energy gap (in units of mK). Normally, $T_s \gg T_\star$, and so the new ζ correction in Eq. (30) approaches 1. When T_s becomes comparable to T_\star , the

¹⁴https://github.com/kboddy/class_public/tree/dmef14.

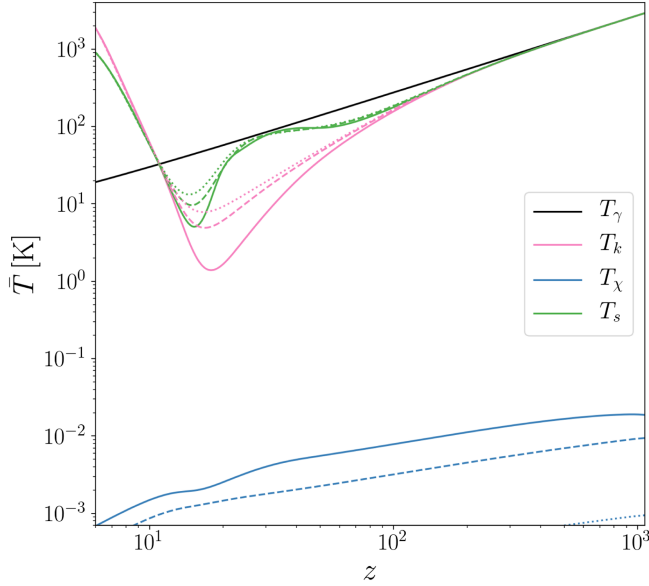


FIG. 9. Evolution of the global gas kinetic temperature, SDM kinetic temperature and the spin temperature, for three different cross sections. Solid, dashed and dotted lines correspond to $\sigma_{-4} = 2 \times 10^{-42}, 10^{-42}, 10^{-43} \text{ cm}^2$, respectively. We note that the T_s solid green curve is most likely too high between $20 \lesssim z \lesssim 30$; see text for further details.

new term becomes important. Yet, because of the following modification, we will see in Sec. VI E that T_s does not become very small even if T_b does.

The Ly α coupling coefficient \tilde{x}_α is proportional to the Ly α flux times a correction factor \tilde{S}_α . In the standard 21cmFAST, \tilde{S}_α is evaluated from the fit of Ref. [128]. This fit becomes inadequate at low temperatures (when $T_b \lesssim 2 \text{ K}$). We therefore follow Ref. [107] and adopt the wing approximation from Refs. [161,162] to evaluate \tilde{S}_α (see more details in Appendix D).

Another modification that has to be done is in the recombination rate α_{rec} . In the standard 21cmFAST, a fit for the case-A recombination rate is used [135]. Again, the validity of this fit breaks at low temperatures. We thus adopt our HyRec scheme that was described in Sec. III (the SDM does not alter the physics of recombination, and so no further modifications in HyRec are required).

Finally, we comment that in 21cmFAST, the collisional coupling x_{coll} is evaluated from tabulated values of κ_{1-0}^{H} . These are the collision rates of hydrogen atoms with species of type i (in units of cm^3/sec). The tabulated values stop at $T_b = 1 \text{ K}$, and the logic of the code is to use $\kappa_{1-0}^{\text{H}}(T_b = 1 \text{ K})$ if $T_b < 1 \text{ K}$. Because the extrapolation to lower temperatures is not trivial and is beyond the scope of this paper, we leave it for future work. Having said that, we emphasize that x_{coll} is mainly relevant during the dark ages, and thus the forecasts we derive in Sec. V (which depend on the physics during cosmic dawn) are insensitive to the exact values of κ_{1-0}^{H} .

D. Small velocity corrections

The contribution of pop-III stars comes from halos that are massive enough to host them. In 21cmFAST, pop-III stars reside in molecular cooling halos, and the aforementioned minimum threshold halo mass is proportional to [86]

$$M_{\text{mol,min}}(x, z) \propto \left[1 + A_{v_{cb}} \frac{V_{cb}(x, z_{\text{rec}})}{\langle V_{cb}^2(z_{\text{rec}}) \rangle^{1/2}} \right]^{\beta_{v_{cb}}}, \quad (31)$$

where $V_{cb}(x, z_{\text{rec}})$ is the relative velocity between baryons and CDM at the time of recombination (obtained in a very similar process to the one outlined in Sec. VI B), and $A_{v_{cb}}, \beta_{v_{cb}} > 0$ are free phenomenological parameters. Note that Eq. (31) is the source for the velocity acoustic oscillations—a standard ruler imprinted on the 21-cm power spectrum at large scales [158,163,164].

In the presence of SDM, there are two dark matter species that hamper pop-III structure formation due to their relative velocities with the baryons—CDM and SDM. We weigh their contributions to $M_{\text{mol,min}}$ in the following way:

$$M_{\text{mol,min}}(x, z) \propto \left\{ 1 + A_{v_{cb}} \left[(1 - f_\chi) \frac{V_{cb}(x, z_{\text{rec}})}{\langle V_{cb}^2(z_{\text{rec}}) \rangle^{1/2}} + f_\chi \frac{V_{\chi b}(x, z)}{\langle V_{cb}^2(z_{\text{rec}}) \rangle^{1/2}} \frac{1 + z_{\text{rec}}}{1 + z} \right] \right\}^{\beta_{v_{cb}}}. \quad (32)$$

The reason for this modeling is because of the following. If $f_\chi = 0$ then Eq. (32) becomes identical to Eq. (31). If $f_\chi \approx 1$, then the second term in Eq. (32) dominates. Note that in the special case of $f_\chi \approx 1$ and very small σ_{-4} , SDM behaves as CDM, $V_{\chi b} \approx V_{cb} \propto (1 + z)$, and Eq. (31) is again restored in that scenario. For cross sections large enough, $V_{\chi b} \ll V_{cb}$ (cf. Fig. 8). Thus, in an SDM universe, Eq. (32) implies that $M_{\text{mol,min}}$ is smaller, and hence more pop-III stars can be born, thereby pulling cosmic dawn to higher redshifts. It is worthwhile to note that the free parameters $A_{v_{cb}}$ and $\beta_{v_{cb}}$ were calibrated in [86] to match with hydrodynamical N-body simulations [165,166]. As fitting our model to such simulations is beyond the scope of this work, we adopt the simple model of Eq. (32) with the same fiducial parameters. We defer the exploration of more complicated prescriptions (where, for instance, the weights f_χ and $1 - f_\chi$ include power laws with free indices) to future work.

The SFRD in 21cmFAST depends both on $M_{\text{mol,min}}$ and on the halo mass function (HMF). The latter is modified by SDM in two ways. First, the matter-density variance $\sigma(M)$ is reduced because of the suppression in the matter power spectrum [107]. And secondly, the fitting function that is used for the evaluation of the HMF is modified. In this work, the former effect is already taken into account in our analysis, while the second is not. We use the Sheth-Tormen fitting function [167], which was calibrated based on CDM

N-body simulations. It is not clear how the fitting parameters of the Sheth-Tormen HMF are modified if SDM is considered instead of CDM. We leave the exploration of this subtlety¹⁵ for future work.

E. Results–SDM

In what follows we will consider three case studies where σ_{-4} is equal to $2 \times 10^{-42} \text{ cm}^2$, 10^{-42} cm^2 or 10^{-43} cm^2 . The impact of these cross sections on the evolution of the baryons and SDM fluids is most clearly seen in Fig. 8 where we plot the “global” $V_{\chi b}$ [see caveat below Eq. (29)]. The green curve that corresponds to $\sigma_{-4} = 10^{-43} \text{ cm}^2$ can be considered as “almost Λ CDM” because $V_{\chi b} \propto (1+z)$, which is indeed the evolution of V_{cb} when there is no drag term in Eq. (20). In contrast, the blue curve of $\sigma_{-4} = 2 \times 10^{-42} \text{ cm}^2$ decays very quickly; initially the Hubble term dominates, then at $z \sim 100$ the drag term wins, and finally at $z \sim 15$ the Hubble term dominates again once $V_{\chi b}$ is small enough. The case of $\sigma_{-4} = 10^{-42} \text{ cm}^2$ (orange curve) exhibits a similar decay, although milder.

Next, we consider the evolution of T_b and T_χ as it appears in Fig. 9. Let us focus first on the solid curves of $\sigma_{-4} = 2 \times 10^{-42} \text{ cm}^2$ where the new physics is most extreme. As expected, the rapid interactions between the baryons and the cold SDM cool down the former considerably. Once stars have been formed, their radiated x rays heat up the gas, as in Λ CDM. Note that the turning point of the pink solid curve appears before the other pink curves; this is because a very cold baryonic gas reacts to the slightest source of heating. In fact, without x rays, the baryons would have been tightly coupled to the SDM at $z \sim 17$ because the interaction rate increases as $V_{\chi b}$ decreases, and $V_{\chi b}$ already approaches zero at low redshifts. As for T_χ , we can see that the Hubble cooling in Eq. (18) mostly dominates with respect to the \dot{Q}_χ heating term. Unlike the baryons, which undergo a lot of SDM scattering, the SDM particles barely feel the baryons. This is because ρ_χ is comparable to ρ_b for $f_\chi = 100\%$. However, their number densities are not; $m_b \approx 1 \text{ GeV} \gg m_\chi$ in the model that we are considering and thus $n_\chi \gg n_b$, namely the SDM particles vastly outnumber the baryons. Nevertheless, the SDM is not completely oblivious to the presence of the baryons, and it begins to heat up at $z \sim 15$ once the temperature difference becomes large enough. Then, at $z \sim 10$ the Hubble cooling wins again, and the SDM is further cooled down. All the physics discussed above applies as well to the dashed and dotted curves in Fig. 9, although to a much lesser extent.

Figure 9 also presents the evolution of the spin temperature. Let us begin the discussion this time with the dashed and dotted curves that correspond to $\sigma_{-4} = 10^{-42} \text{ cm}^2$ and $\sigma_{-4} = 10^{-43} \text{ cm}^2$, respectively. It appears that the WF coupling is stronger for the dashed curve, and thus the cosmic dawn allegedly arrives earlier when the cross section is larger. In the SDM model there are many factors that affect the onset of cosmic dawn. For example, as Ref. [107] pointed out, the matter power spectrum is suppressed on small scales due to the presence of the SDM. This fact contributes to the delaying of cosmic dawn (in a mechanism similar to that in FDM [96,97]). However, there are other competing effects. First, since $T_\alpha \approx T_k$, smaller T_k tends to drive T_s to smaller values (note however that this effect has nothing to do with the onset of cosmic dawn). Secondly, the lower $V_{\chi b}$ values imply a smaller $M_{\text{mol,min}}$ [cf. Eq. (32)], which means that smaller halos (that are much more abundant) can form stars more easily. On the other hand, there are two more effects that tend to weaken the coupling of T_k to T_s for larger cross sections: (1) Smaller T_k implies smaller \tilde{S}_α (see Appendix D), and (2) smaller $M_{\text{mol,min}}$ leads to a stronger LW radiation that impedes star formation (although the LW feedback effect may yield a weaker LW flux, so it is not clear *a priori* if this effect enhances or degrades the coupling of T_s to T_k). All in all, we find that for the model that we are considering,¹⁶ T_s is more strongly coupled to T_k when the cross section is larger.

As for the solid green curve in Fig. 9, the similar trend continues. For the fiducial parameters we have used, we find that cross sections larger than $\sigma_{-4} = 2 \times 10^{-42} \text{ cm}^2$ can result in extremely low temperatures that reach below $T_k = 1 \text{ K}$. As was discussed at the end of Sec. VIC, 21cmFAST interpolates a table of κ_{1-0}^{H} that has no entries below $T_k = 1 \text{ K}$. Thus, unless the interpolation table of 21cmFAST is extended to lower temperatures, larger cross sections may yield unphysical behaviors at the T_s curve.

It is also interesting to inspect the evolution of x_e in an SDM universe. For $\sigma_{-4} = 10^{-42} \text{ cm}^2$ and $\sigma_{-4} = 10^{-43} \text{ cm}^2$, Fig. 10 shows that SDM barely makes any difference in the evolution of x_e compared to Λ CDM. However, a surprising feature can be seen when we consider $\sigma_{-4} = 2 \times 10^{-42} \text{ cm}^2$; at $z \sim 40$ we see that x_e departs from the Λ CDM expectation toward lower values. Normally, in Λ CDM the temperature of the baryons at this redshift is insufficient to allow an efficient recombination, because their number density is too low. But for the SDM that we are considering, recombination becomes efficient again at $z \sim 40$ because baryons are combined into atoms more easily when the temperature decreases. Without x-ray heating, we find that

¹⁵We thank Mihir Kulkarni for drawing our attention to this assumption in our analysis.

¹⁶We did witness a weaker WF coupling with much stronger cross sections, or when we considered $m_\chi = 1 \text{ GeV}$.

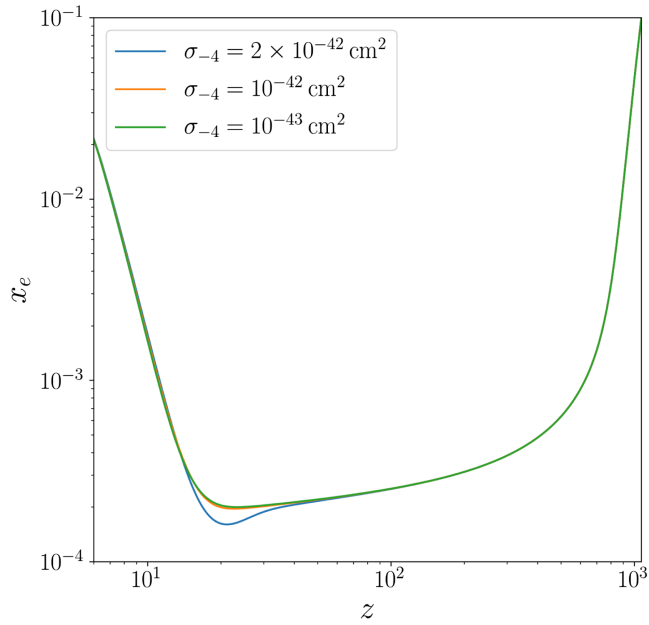


FIG. 10. Evolution of the global x_e in the SDM universe, for three different cross sections. The green curve of $\sigma_{-4} = 10^{-43} \text{ cm}^2$ is practically indistinguishable from the ΛCDM curve shown in Fig. 3. The extra drop seen in the blue curve of $\sigma_{-4} = 2 \times 10^{-42} \text{ cm}^2$, although it can be physically justified, is subject to theoretical uncertainties; see main text for more details.

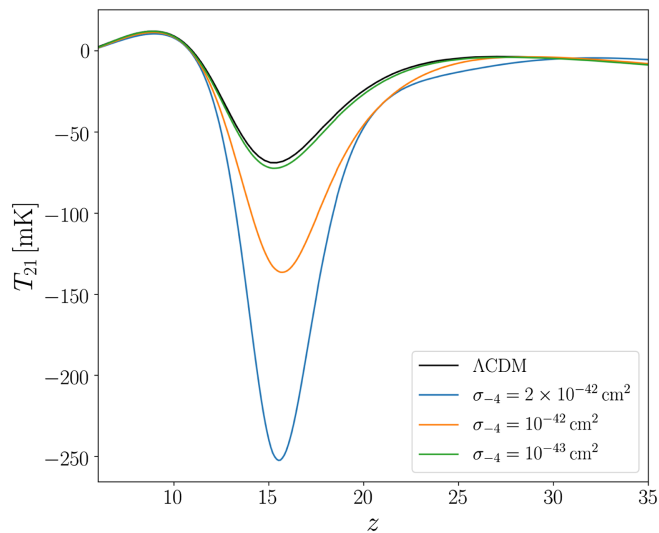


FIG. 11. The global 21cm signal in the SDM universe, for three different cross sections.

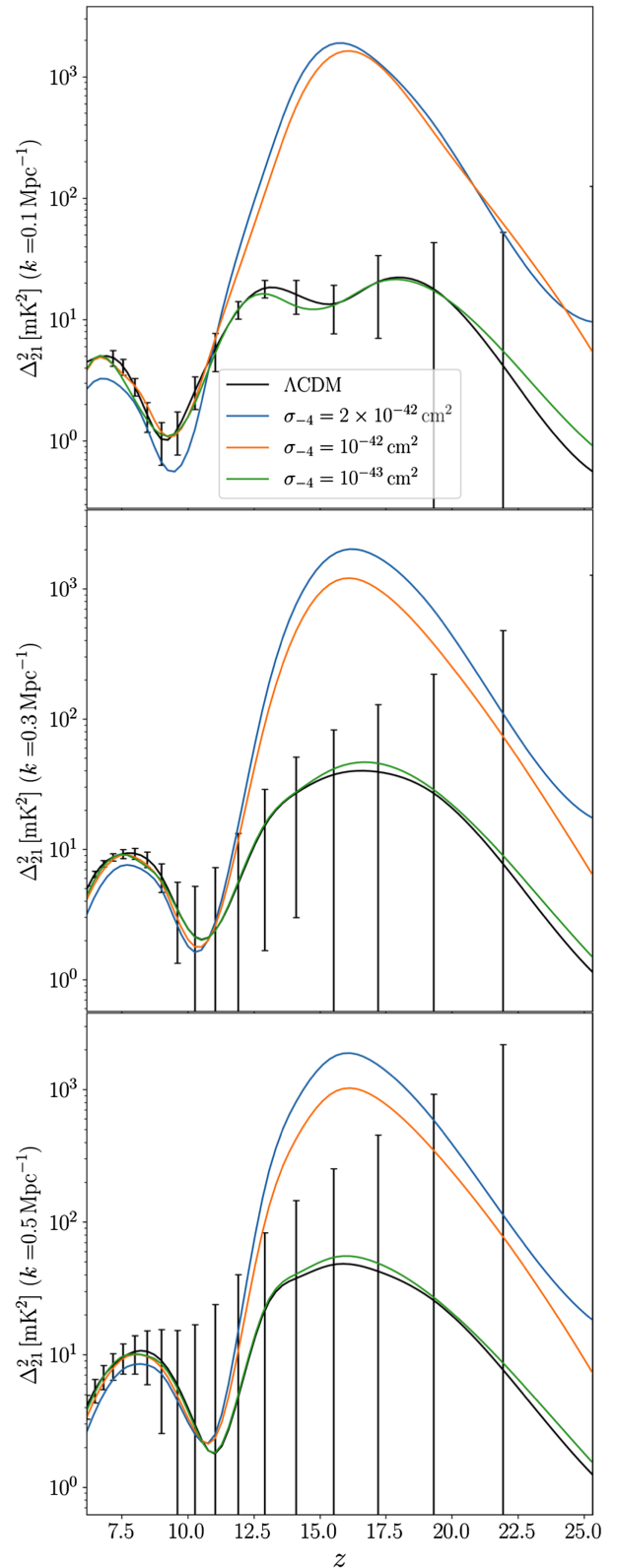


FIG. 12. The 21-cm power spectrum in SDM universe, for three different cross sections. Here, unlike Fig. 5, we assume moderate foreground scenario for the error bars.

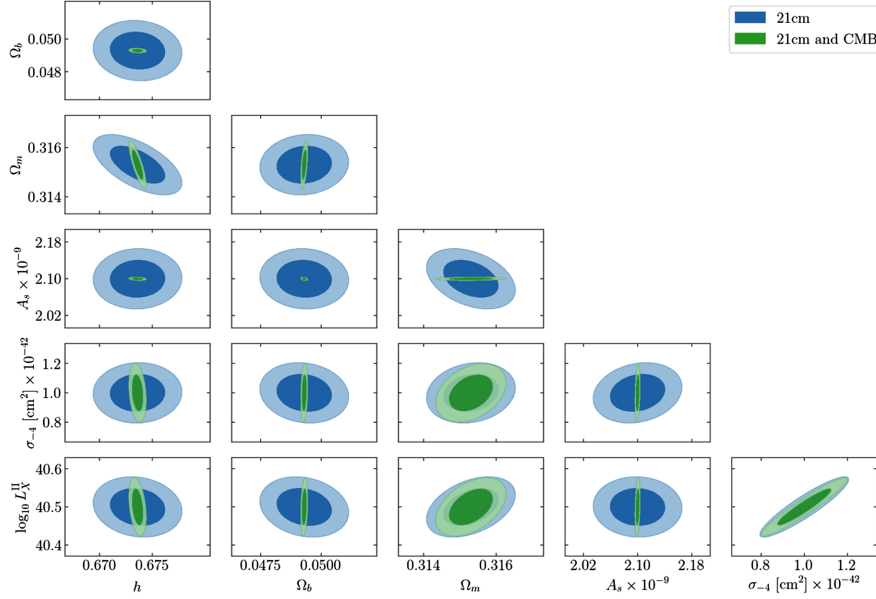


FIG. 13. Forecasts of 1- σ and 2- σ confidence levels of some of the free parameters in Eq. (12) and the SDM cross section σ_{-4} (the rest of the parameters not shown here have been marginalized), while imposing Planck 2018 priors [40] on the Λ CDM cosmological parameters. Blue ellipses correspond to forecasts when only information from HERA is considered, while the green ellipses account for information coming from CMB-S4 as well. Results are shown for a moderate foreground scenario, although they barely change when a pessimistic foreground scenario is considered.

for this scenario x_e would stabilize on a lower freeze-out value of $\sim 2 \times 10^{-6}$. Yet, it is important to stress that at low temperatures HyRec uses the fit of Ref. [168] for the recombination rate, but this fit is valid only to $T_k = 40$ K, so the second drop in x_e shown in Fig. 10 should not be taken too seriously.

The global 21-cm signal, shown in Fig. 11, reflects the same physics previously discussed. Larger cross sections lead to a deeper absorption signal that begins at higher redshifts, but ends roughly at the same redshift. We show the corresponding 21-cm power spectrum in Fig. 12. It can be clearly seen that HERA will not be able to distinguish between Λ CDM and SDM of cross section $\sigma_{-4} = 10^{-43}$ cm². In contrast, it appears that HERA will be able to easily detect SDM with cross section $\sigma_{-4} = 10^{-42}$ cm² (or higher) but only in the low frequency band that corresponds to $10 \lesssim z \lesssim 20$. Two remarks on the blue curve of $\sigma_{-4} = 2 \times 10^{-42}$ cm²: (1) Although its global signal reaches much lower values than the orange curve of $\sigma_{-4} = 10^{-42}$ cm², the amplitude of the 21-cm power spectrum for both cross sections is of the same order of magnitude. This is most likely because the absorption profile of $\sigma_{-4} = 2 \times 10^{-42}$ cm² is quite narrow, and we calculate the power spectrum from slices of the light cone box, which unlike the coeval box contains samples from different redshifts along the line of sight. (2) The smaller power at low redshifts is due to a shallower emission profile which is caused by the large cooling effect.

F. Forecasts–SDM

Figure 12 suggests that HERA will not be sensitive to cross sections below 10^{-43} cm², but cross sections of the order of 10^{-42} cm² or higher can be probed. Yet, all we did in Fig. 12 was to vary the cross section while keeping other parameters fixed. If we wish to forecast the sensitivity of HERA to SDM, we must vary other cosmological and astrophysical parameters and study their degeneracies, like we did in Sec. V. For the following analysis, we focus on the SDM scenario where $\sigma_{-4} = 10^{-42}$ cm². This particular value has not been ruled out by Planck 2018 CMB measurements, and it lies beyond the sensitivity range of CMB-S4 by almost an order of magnitude [101,103].

Our forecasts are displayed in Fig. 13. Interestingly, the forecasts for Ω_m seem to be less affected when combining the information from the two observables. We will see why shortly. Furthermore, we see a strong degeneracy between σ_{-4} and $L_X^{(\text{II})}$. This feature in our forecasts is not surprising; stronger σ_{-4} yields more efficient cooling, while stronger $L_X^{(\text{II})}$ yields more efficient heating; thereby any small correlated variation in both of them is almost canceled in the observed brightness temperature. Hence, these two parameters exhibit a positive correlation. Since the CMB anisotropies do not depend on the value of $L_X^{(\text{II})}$, their measurement cannot relax this degeneracy.

It is also interesting to compare HERA’s performance in detecting SDM with CMB-S4. We make this comparison

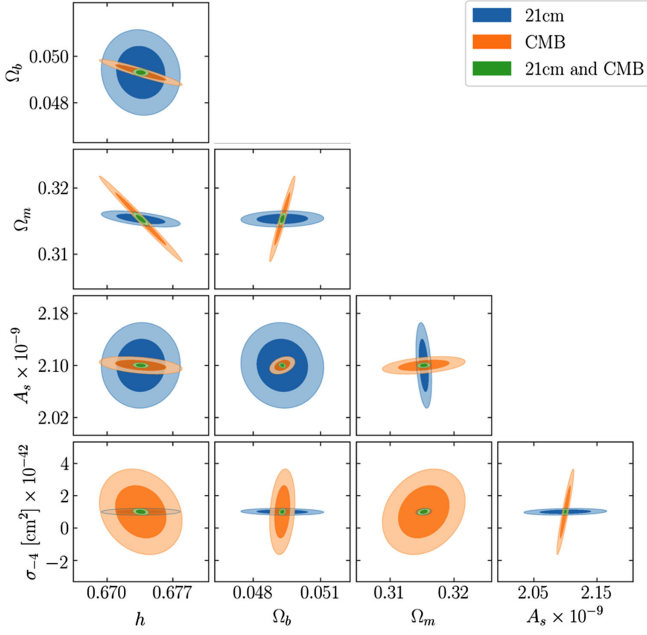


FIG. 14. Forecasts of 1- σ and 2- σ confidence levels of the free cosmological parameters in Eq. (12) and the SDM cross section σ_{-4} , while imposing Planck 2018 priors [40] on the Λ CDM cosmological parameters. The assumptions made in this figure are similar to those of Fig. 13, but here we have marginalized over all astrophysical parameters, allowing us to present forecasts for only CMB-S4. Blue (orange) ellipses correspond to forecasts when only information from HERA (CMB-S4) is considered, while the green ellipses account for information coming from both HERA and CMB-S4. All the astrophysical parameters have been marginalized (fixed) in the calculation of the HERA (CMB-S4) Fisher matrix. For HERA, results are shown for the moderate foreground scenario, although they barely change when a pessimistic foreground scenario is considered.

in Fig. 14. As we saw in Fig. 7 when we discussed degeneracies in Λ CDM, for most cosmological parameters CMB-S4 has a better constraining power than HERA. However, in the SDM scenario, HERA has the upper hand when it comes to constraining Ω_m (which is now comprised of SDM, unlike in Λ CDM) and σ_{-4} . In particular, for SDM with $\sigma_{-4} = 10^{-42} \text{ cm}^2$, HERA will be able to constrain its value within a 2- σ confidence level, while CMB-S4 will barely be able to do so within a 1- σ confidence level. This demonstrates the potential of HERA in detecting new physics that cannot be probed by CMB-S4.

VII. CONCLUSIONS

In this paper we have introduced our novel pipeline, 21cmFirstCLASS, for studying the cosmological 21-cm signal and its anisotropies. It is composed of two codes that are commonly used in the literature—CLASS and 21cmFAST. Because CLASS provides the proper initial conditions for the simulation, as well as the more precise scale-independent growth factor, our code in that sense is more

consistent than the standard 21cmFAST. Moreover, since our simulation begins from recombination, our calculations naturally capture early temperature and ionization fluctuations, an effect which distorts the 21-cm power spectrum to some extent¹⁷ (cf. Fig. 5). To achieve the most precise evolution of the early Universe, we have incorporated in 21cmFirstCLASS the state-of-the-art recombination code HyRec as an integral part of our calculation.

Unlike 21cmFAST, our code is *not* fast. For the box settings we used in this work, starting the simulation at recombination results in a run-time which is ~ 3 times longer compared to the normal 21cmFAST simulation that begins at $z = 35$, even though no complicated astrophysics calculations are performed at high redshifts. The run-time ratio becomes even greater when either SDM (which requires more redshift samples below $z = 35$) or higher resolution boxes are considered. The source for this longer run-time is the huge amount of redshift samples used in 21cmFirstCLASS and the current architecture of 21cmFAST; at each redshift iteration the evolution of the box is done at the C level (where multiple CPUs can facilitate the computation), but at the end of the iteration the box is transferred back to the Python wrapper, where the box can be processed with only a single CPU. We therefore think that changing the 21cmFAST architecture such that the C code will be able to promote the box over more than one redshift iteration may speed up significantly the calculations of 21cmFirstCLASS. Implementing this is beyond the scope of this paper, and we defer this necessary modification to future work.

One of the main motivations to begin the simulation from recombination is to study highly nonlinear models. As a case study, we focused on SDM, which is one of the most popular candidates of dark matter in the recent literature. This required us using the modified CLASS version of Ref. [101] to get the correct initial conditions. Moreover, besides implementing the SDM differential equations in 21cmFAST, we had to make several modifications in the astrophysics part; the most important one is the correction factor \tilde{S}_α for the WF coupling. As a first thorough study of the effect that SDM has on the 21-cm power spectrum, we limited ourselves to SDM with parameters $f_\chi = 100\%$, $m_\chi = 1 \text{ MeV}$ and a velocity-dependent cross section with a power law of $n = -4$. For very large cross sections that change the 21-cm signal extremely, our results suffer from an inconsistency at $z \gtrsim 20$ due to an approximated modeling of the collisional rates κ_{1-0}^{iH} at low temperatures. For milder cross sections, our results are consistent at all redshifts.

Focusing on $\sigma_{-4} = 10^{-42} \text{ cm}^2$, which on the one hand has not been ruled out by Planck 2018 measurements, but on the other hand lies beyond the CMB-S4 sensitivity

¹⁷We elaborate more on that subtle point in Paper II.

range, we found that HERA in its design sensitivity will be able to easily probe SDM with that cross section within a $2\text{-}\sigma$ confidence level, under the assumption of either moderate or pessimistic foreground scenarios, and taking the degeneracies with astrophysical parameters into account. This serves as clear evidence to the very promising potential of HERA and the 21-cm signal in searching for signatures of physics beyond ΛCDM , provided that state-of-the-art, first-class codes are used.

ACKNOWLEDGMENTS

It is our pleasure to thank Bradley Greig, Julian B. Muñoz, Kimberly K. Boddy, Sarah Libanore, Manuel A. Buen-Abad, Hovav Lazare and Gali Shmueli for useful discussions. Furthermore, we would like to thank the anonymous referee for useful comments that improved the quality of the paper. We also acknowledge the efforts of the 21cmFAST and CLASS authors to produce state-of-the-art public 21-cm and CMB codes. J. F. is supported by the Zin fellowship awarded by the BGU Kreitmann School. E. D. K. acknowledges support from an Azrieli faculty fellowship. E. D. K. also acknowledges joint support from the U.S.-Israel Bi-national Science Foundation (BSF, Grant No. 2022743) and the U.S. National Science Foundation (NSF, Grant No. 2307354), and support from the ISF-NSFC joint research program (Grant No. 3156/23).

APPENDIX A: SCALE-INDEPENDENT GROWTH FACTOR

Because CDM is collisionless and comprises most of the matter in the Universe, its evolution is nearly scale invariant (especially at high redshifts before baryons have clustered), and thus the growth in its density contrast is given by $\delta_c(k, z) = D(z)\delta_c(k, z=0)$, where $D(z)$ is the scale-independent growth factor. Using the continuity and Euler equations, together with the Poisson equation, one can show that the differential equation that governs $D(z)$ is [169]

$$\ddot{D} + 2H\dot{D} - 4\pi G\bar{\rho}_m D = 0, \quad (\text{A1})$$

where G is Newton's gravitational constant and overdots represent derivatives with respect to the cosmological time t .

Among its calculations, CLASS solves Eq. (A1) to find $D(z)$. In contrast, 21cmFAST does not solve Eq. (A1), and instead it adopts the fit of Refs. [137,138], known in the code as the Dicke growth factor. In Fig. 15 we show the two growth factors of the two codes. The agreement between them becomes excellent at low redshifts, although percent-level errors can still be found for $z \gtrsim 20$. At high redshifts, the error of the Dicke fit is no longer negligible, and it reaches $\sim 20\%$ at $z = 1000$. In order to simulate early temperature and ionization fluctuations as

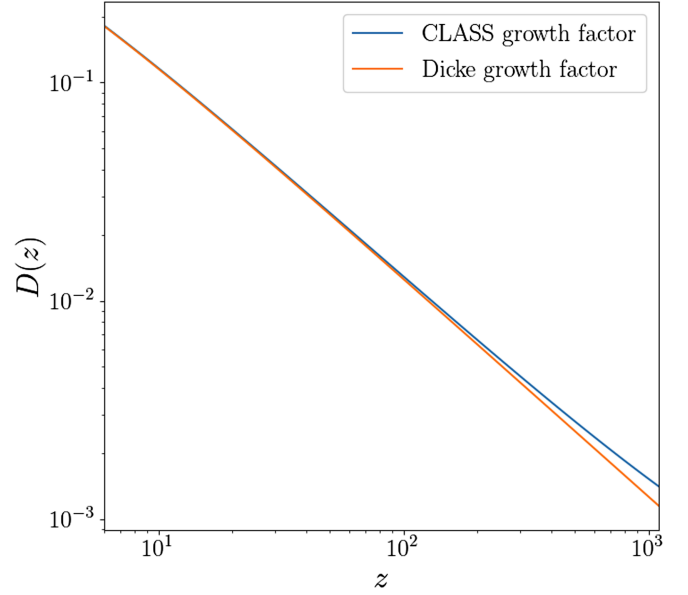


FIG. 15. Comparison between the CLASS growth factor [which solves Eq. (A1)] and the Dicke growth factor, as implemented in the standard 21cmFAST. At $z = 35$ ($z = 20$) the relative error is $\sim 1.4\%$ ($\sim 0.98\%$).

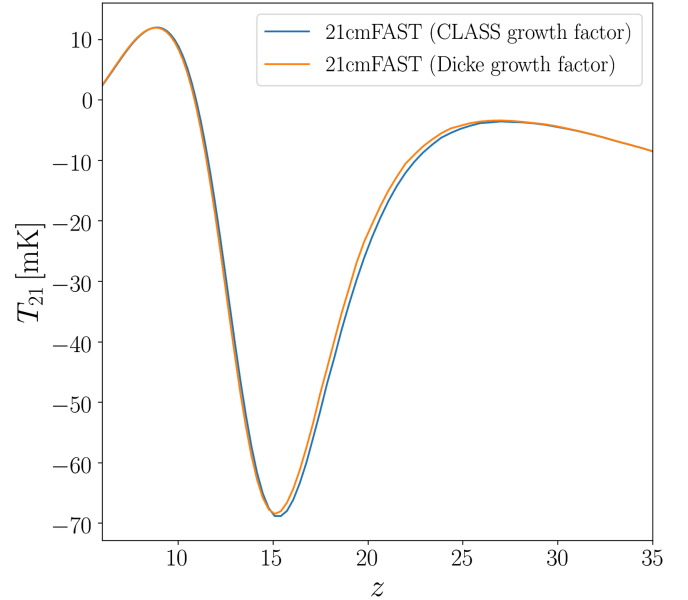


FIG. 16. Comparison of the 21-cm global signal when different growth factors are considered. In both curves early temperature and ionization fluctuations were discarded by starting the simulation at $z = 35$.

precisely as possible (see more on them in Paper II), we therefore had to incorporate the CLASS growth factor in 21cmFirstCLASS.

It is interesting however that the small errors of the Dicke fit below $z = 35$ can lead to a visible difference in the 21-cm global signal, even if early temperature and ionization fluctuations are discarded, as we show in Fig. 16.

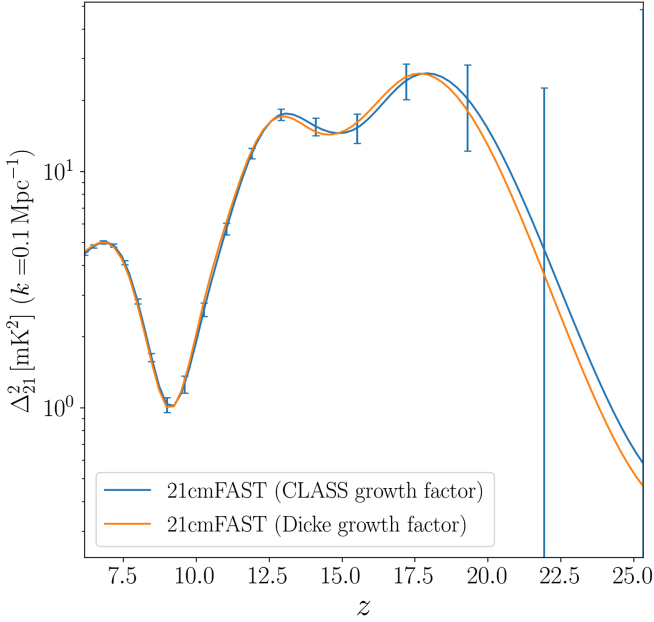


FIG. 17. Comparison of the 21-cm power spectrum when different growth factors are considered. In both curves early temperature and ionization fluctuations were discarded by starting the simulation at $z = 35$. Optimistic foreground scenario is assumed for the error bars.

Above $z \sim 27$, the resulting global signal is the same because at this epoch the fluctuations are linear and they cancel each other when the mean of the box is evaluated. Below that redshift, nonlinearities become important and the fluctuations (as well as the errors) are no longer canceled. At $z \lesssim 15$ the SFRD dominates the fluctuations in the signal, and because the growth factors are nearly the same at that redshift, the Dicke solution to the global brightness temperature coincides with the CLASS solution.

The errors induced by the Dicke growth factor are enhanced when the 21-cm power spectrum is considered, especially at $z \gtrsim 20$, as can be seen in Fig. 17. Yet, within HERA's range, the errors do not surpass HERA's noise level.

APPENDIX B: COMPTON TIGHT COUPLING APPROXIMATION

As was discussed in Sec. III B, above $z = 980$ the temperature cannot be evolved precisely if one attempts to solve Eq. (3) numerically via the Euler method but without having a tiny step size. The reason for this comes from the Compton term in Eq. (3). At high redshifts this term dominates, leading to $dT_k/dz \propto (\Gamma_C/H)(T_\gamma - T_k)$. Since the baryons are tightly coupled to the photons at this epoch, $T_k \rightarrow T_\gamma$. However, because $\Gamma_C \gg H$, small initial errors in T_k could cause the solution to overshoot or undershoot T_γ , depending on the sign of $T_\gamma - T_k$, with

oscillations that grow in time. This numerical behavior is well known for interacting fluids in the tight coupling regime. It becomes worse when the temperatures of both fluids have to be simultaneously evolved in time—see Appendix C.

To overcome this challenge, many codes use more advanced numerical schemes such as having an adaptive varying step size or using values from more past samples instead of just the last one. In 21cmFAST we cannot use such schemes because the redshift samples (and their corresponding step sizes) are determined before the evolution of the box begins, and only the last previous box is accessible during the calculation of the current one. Therefore, our numerical scheme is limited to the family of Runge-Kutta solutions. High order Runge-Kutta solutions could increase the required step size at the price of calculating intermediate redshift samples, but we will see that the simplest lowest-order type of Runge-Kutta solution, namely the Euler method, can still be used without sacrificing valuable computational time.

The trick is to track the difference and the average temperatures of the tightly coupled fluids, instead of tracking the temperatures of the individual fluids. A similar method to the one presented below is already implemented in CLASS. To see why such a method is helpful, let us rewrite Eq. (17) (that also includes interaction with SDM) in the following form (note we now denote the kinetic gas temperature with T_b to match our notation in Sec. VI):

$$\frac{dT_b}{dz} = \frac{1}{1+z} \left[2T_b - \frac{T_\gamma - T_b}{\epsilon_{\gamma b}} - \frac{2\dot{Q}_b}{3k_B H} - \frac{1}{H} \frac{dT_b}{dt} \Big|_{\text{ext}} \right], \quad (\text{B1})$$

where we defined $\epsilon_{\gamma b} \equiv H/\Gamma_C$. Because $T_\gamma \propto (1+z)$, we also know that

$$\frac{dT_\gamma}{dz} = \frac{T_\gamma}{1+z}. \quad (\text{B2})$$

When the two fluids are tightly coupled, we approximate $T_b \approx T_\gamma + \mathcal{O}(\epsilon_{\gamma b})$, which is valid as long as $H \ll \Gamma_C$, or $\epsilon_{\gamma b} \ll 1$. This is the Compton TCA. Within this approximation, we can compare Eqs. (B1) and (B2),

$$T_\gamma = 2T_b - \frac{T_\gamma - T_b}{\epsilon_{\gamma b}} - \frac{2\dot{Q}_b}{3k_B H} - \frac{1}{H} \frac{dT_b}{dt} \Big|_{\text{ext}} + \mathcal{O}(\epsilon_{\gamma b}), \quad (\text{B3})$$

from which we find

$$\begin{aligned} \Delta T_{\gamma b} &\equiv T_\gamma - T_b \\ &= \epsilon_{\gamma b} \left[2T_b - T_\gamma - \frac{2\dot{Q}_b}{3k_B H} - \frac{1}{H} \frac{dT_b}{dt} \Big|_{\text{ext}} \right] + \mathcal{O}(\epsilon_{\gamma b}^2). \end{aligned} \quad (\text{B4})$$

Furthermore, by adding Eqs. (B1) and (B2) we can find a differential equation for $\bar{T}_{\gamma b} \equiv (T_\gamma + T_b)/2$,

$$\begin{aligned} \frac{d\bar{T}_{\gamma b}}{dz} &= \frac{1}{2(1+z)} \left[T_\gamma + 2T_b - \frac{T_\gamma - T_b}{\epsilon_{\gamma b}} - \frac{2\dot{Q}_b}{3k_B H} - \frac{1}{H} \frac{dT_b}{dt} \Big|_{\text{ext}} \right] \\ &= \frac{T_\gamma}{1+z} + \mathcal{O}(\epsilon_{\gamma b}), \end{aligned} \quad (\text{B5})$$

where the second line follows Eq. (B3). Not surprisingly, we see that the average temperature of the tightly coupled baryon-photon fluid follows the CMB temperature. We would need a second differential equation, for the temperature difference $\Delta T_{\gamma b}$. According to Eq. (B4), this is equivalent to finding a differential equation for $\epsilon_{\gamma b}$. From Eqs. (4) and (B2), a simple calculation yields

$$\frac{d\epsilon_{\gamma b}}{dz} = \epsilon_{\gamma b} \left(\frac{1}{H} \frac{dH}{dz} - \frac{1}{x_e(1-x_e)} \frac{dx_e}{dz} - 4 \right). \quad (\text{B6})$$

Equations (B4)–(B6) are the Compton-TCA equations. Unlike Eqs. (3) or (17), they do not contain terms that approach zero or infinity in the strong coupling limit, and they are thus numerically more stable. The strategy in our code for solving for T_b is as follows:

- (1) At each step, we calculate $\epsilon_{\gamma b} \equiv H/\Gamma_C$. If $\epsilon_{\gamma b} > \epsilon_{\gamma b}^{\text{th}}$, where $\epsilon_{\gamma b}^{\text{th}}$ is some threshold value, the TCA does not have to be applied, and we solve Eq. (3).
- (2) Otherwise, we compute $\bar{T}_{\gamma b}$, and evolve $\bar{T}_{\gamma b}$ and $\epsilon_{\gamma b}$ via Eqs. (B5) and (B6), respectively.
- (3) We then compute the current $\Delta T_{\gamma b}$ via Eq. (B4).
- (4) Finally, we find the current gas temperature with $T_b = \bar{T}_{\gamma b} - \Delta T_{\gamma b}/2$.

With this prescription, we can run `21cmFirstCLASS` with a constant $\Delta z_n = 0.1$ from recombination to $z = 35$ and thus reduce the total amount of redshift samples by ~ 8000 . In our code we have set $\epsilon_{\gamma b}^{\text{th}} = 5 \times 10^{-5}$ since this choice corresponds to $\epsilon_{\gamma b}(z = 980) \approx \epsilon_{\gamma b}^{\text{th}}$, though we comment that $\epsilon_{\gamma b}^{\text{th}}$ can be even 3 orders of magnitude greater, and the desired evolution would be still obtained.

APPENDIX C: DARK MATTER TIGHT COUPLING APPROXIMATION

A similar problem to the one discussed in Appendix B happens when baryons interact with SDM. According to Eqs. (17) and (18), the changes in T_b and T_χ depend on \dot{Q}_b and \dot{Q}_χ , but according to Eqs. (24) and (25), these quantities depend on the difference between T_b and T_χ . If $\Gamma_{\chi b} \gg H$ [or $(n_b/n_\chi)\Gamma_{\chi b} \gg H$], then $T_b - T_\chi \rightarrow 0$ and small numerical deviations from the true solution will cause the error to diverge, in both fluids. Moreover, it becomes unclear what happens in a scenario where the fluids are tightly coupled, but only one of them is strongly affected by an external source, e.g. x rays that only heat up the baryon fluid. This is why the DM-TCA algorithm that we derive below does not serve only as a means to reduce run-time,

but in fact it is *indispensable* to get the right evolution at low redshifts.

We begin by rewriting Eqs. (17) and (18) in the following form:

$$\begin{aligned} \frac{1}{H} \frac{dT_b}{dt} &= -2T_b + \frac{T_\gamma - T_b}{\epsilon_{\gamma b}} + \frac{T_\chi - T_b}{\epsilon_b} + \frac{1}{H} \frac{dT_b}{dt} \Big|_{\text{ext}} \\ &\quad + \frac{2}{3k_B \rho_{\text{tot}}} \frac{\rho_\chi V_{\chi b}}{H} \sum_t \frac{m_\chi m_b}{m_\chi + m_t} D_t(V_{\chi b}), \end{aligned} \quad (\text{C1})$$

$$\begin{aligned} \frac{1}{H} \frac{dT_\chi}{dt} &= -2T_\chi + \frac{T_b - T_\chi}{\epsilon_\chi} + \frac{1}{H} \frac{dT_\chi}{dt} \Big|_{\text{ext}} \\ &\quad + \frac{2}{3k_B \rho_{\text{tot}}} \frac{\rho_b V_{\chi b}}{H} \sum_t \frac{m_\chi m_t}{m_\chi + m_t} D_t(V_{\chi b}), \end{aligned} \quad (\text{C2})$$

where we have defined the DM-TCA small parameters,

$$\epsilon_b \equiv \frac{H}{\Gamma_{\chi b}}, \quad \epsilon_\chi \equiv \frac{n_\chi}{n_b} \epsilon_b. \quad (\text{C3})$$

It will be convenient to define a symmetrized small parameter,

$$\begin{aligned} \epsilon_{\chi b} &\equiv \frac{n_\chi}{n_\chi + n_b} \epsilon_b = \frac{n_b}{n_\chi + n_b} \epsilon_\chi \\ &= \frac{3H}{\sqrt{2\pi} \sigma_{-4} c^4 (n_\chi + n_b)} \left[\sum_t \frac{n_t}{n_b} \frac{m_t e^{-r_t^2/2}}{(m_t + m_\chi)^2 u_{\chi t}^3} \right]^{-1}. \end{aligned} \quad (\text{C4})$$

In the DM-TCA we have $\epsilon_{\chi b} \ll 1$ and $T_b = T_\chi + \mathcal{O}(\epsilon_{\chi b})$. This allows us to compare Eqs. (C1) and (C2), and find that in the strong coupling limit the temperature difference is

$$\begin{aligned} \Delta T_{b\chi} &\equiv T_b - T_\chi = \epsilon_{\chi b} \left[\frac{T_\gamma - T_b}{\epsilon_{\gamma b}} + \frac{1}{H} \frac{dT_b}{dt} \Big|_{\text{ext}} - \frac{1}{H} \frac{dT_\chi}{dt} \Big|_{\text{ext}} \right. \\ &\quad \left. - \frac{2}{3k_B} \frac{V_{\chi b} m_\chi}{H \rho_{\text{tot}}} \sum_t \frac{\rho_b m_t - \rho_\chi m_b}{m_\chi + m_t} D_t(V_{\chi b}) \right] + \mathcal{O}(\epsilon_{\chi b}^2). \end{aligned} \quad (\text{C5})$$

By adding together Eqs. (C1) and (C2), and using Eq. (C5), we can also find a differential equation for $\bar{T}_{\chi b} \equiv (T_b + T_\chi)/2$,

$$\begin{aligned} \frac{d\bar{T}_{\chi b}}{dz} &= \frac{1}{1+z} \left[2\bar{T}_{\chi b} - \frac{n_b}{n_b + n_\chi} \left(\frac{T_\gamma - T_b}{\epsilon_{\gamma b}} + \frac{1}{H} \frac{dT_b}{dt} \Big|_{\text{ext}} \right) \right. \\ &\quad \left. - \frac{n_\chi}{n_b + n_\chi} \frac{1}{H} \frac{dT_\chi}{dt} \Big|_{\text{ext}} - \frac{1}{n_b + n_\chi} \frac{2}{3k_B} \frac{\rho_b \rho_\chi}{H \rho_{\text{tot}}} \right. \\ &\quad \left. \times V_{\chi b} D(V_{\chi b}) \right] + \mathcal{O}(\epsilon_{\chi b}). \end{aligned} \quad (\text{C6})$$

To solve for T_b and T_χ we require another equation for $\Delta T_{b\chi}$. According to Eq. (C5), this is equivalent to having an

equation for $\epsilon_{\chi b}$. Since $n_b \propto n_\chi \propto (1+z)^3$, then from Eqs. (C3) and (C4) we have

$$\frac{d\epsilon_{\chi b}}{dz} = \frac{d\epsilon_b}{dz} = \epsilon_b \left(\frac{1}{H} \frac{dH}{dz} - \frac{1}{\Gamma_{\chi b}} \frac{d\Gamma_{\chi b}}{dz} \right), \quad (\text{C7})$$

where the derivative of the energy transfer rate $\Gamma_{\chi b}$ can be evaluated from its definition, Eq. (26),

$$\begin{aligned} \frac{d\Gamma_{\chi b}}{dz} = & \sqrt{\frac{2}{\pi}} \frac{2\sigma_{-4} c^4 \rho_\chi}{3n_b} \sum_t \left\{ \frac{\rho_t e^{-r_t^2/2}}{(m_t + m_\chi)^2 u_{\chi t}^3} \left[\frac{3}{1+z} - \frac{r_t}{u_{\chi t}} \right. \right. \\ & \left. \left. \times \frac{dV_{\chi b}}{dz} - (3 - r_t^2) \frac{m_t + m_\chi}{m_t m_\chi} \frac{k_B}{u_{\chi t}^2} \frac{d\bar{T}_{\chi b}}{dz} \right] \right\}. \quad (\text{C8}) \end{aligned}$$

Note that $d\Gamma_{\chi b}/dz \propto \Gamma_{\chi b}$ in the special case in which the SDM interacts with a single type of particles.

Equations (C5)–(C8) are the DM-TCA equations. It is crucial to understand that if $\epsilon_{\chi b} \ll 1$, that does not guarantee that both ϵ_b and ϵ_χ are much smaller than unity. This is because $\epsilon_b \propto \rho_\chi^{-1}$ and $\epsilon_\chi \propto \rho_t^{-1}$. So for example, if $f_\chi \ll 1$ such that $\epsilon_b \gg 1$, then the baryons are not tightly coupled to the SDM. However, if σ_{-4} is large enough, then even if $f_\chi \ll 1$, it might be that $\epsilon_\chi \ll 1$ and the SDM is coupled to the baryons. This is similar to the early coupling between baryons and CMB photons; the latter outnumber the former, and thus the baryons are tightly coupled to the CMB, while the CMB photons are insensitive to the baryons. Since $\epsilon_{\chi b} \leq \epsilon_\chi, \epsilon_b$, if either $\epsilon_b \ll 1$ or $\epsilon_\chi \ll 1$, that implies that $\epsilon_{\chi b} \ll 1$, and we can evolve $\bar{T}_{\chi b}$ and $\Delta T_{b\chi}$ with the DM-TCA equations we formulated above.

All of these considerations have been implemented in 21cmFirstCLASS. Below we present the algorithm we use in our code to solve for T_b and T_χ .

- (1) We begin by calculating ϵ_b and ϵ_χ via Eq. (C3). If at least one of them is smaller than the threshold $\epsilon_{\chi b}^{\text{th}}$, we use the DM-TCA equations, Eqs. (C5)–(C8), to find the updated values of $\bar{T}_{\chi b}$ and $\Delta T_{b\chi}$.
 - (a) When we use the DM-TCA equations, we check if $\epsilon_{\gamma b} < \epsilon_{\gamma b}^{\text{th}}$. If this condition is satisfied, we are in the special scenario where the three fluids (baryons, SDM and CMB photons) are strongly coupled. In this case we evaluate $(T_\gamma - T_b)/\epsilon_{\gamma b}$ that appears in Eqs. (C5) and (C6) with the Compton-TCA [Eq. (B4)].
- (2) Next, we solve for the baryon temperature T_b .
 - (a) We check if $\epsilon_{\gamma b} > \epsilon_{\gamma b}^{\text{th}}$ and $\epsilon_b > \epsilon_{\chi b}^{\text{th}}$. If these two conditions are satisfied, or alternatively $dT_b/dt|_{\text{ext}} > 2\dot{Q}_b/(3k_B)$, we solve the usual differential equation for T_b , Eq. (17). The latter condition reflects the understanding that the baryons cannot be tightly coupled to the SDM if an external heating source, such as x rays, is more dominant.

- (b) Otherwise, if $\epsilon_{\gamma b} \leq \epsilon_{\gamma b}^{\text{th}}$, we use the Compton-TCA equations, Eqs. (B4)–(B6), to solve for T_b . This reflects our assumption that the coupling of the baryons with the SDM cannot be stronger than the coupling of the baryons with the CMB. Cross sections that break this assumption imply that $T_b \neq T_\gamma$ at recombination and have been ruled out by CMB observations.

- (c) Otherwise, the baryons are not tightly coupled to the CMB, but they are tightly coupled to the SDM, and we can use $\bar{T}_{\chi b}$ and $\Delta T_{b\chi}$ that we obtained in item 1 to find T_b via $T_b = \bar{T}_{\chi b} + \Delta T_{b\chi}/2$.

- (3) Finally, we solve for the SDM temperature T_χ .
 - (a) We check if $\epsilon_\chi > \epsilon_{\chi b}^{\text{th}}$ or if $dT_\chi/dt|_{\text{ext}} > 2\dot{Q}_\chi/(3k_B)$ (the latter condition can be satisfied at low redshifts, when the clustering of SDM becomes important). If one of these conditions is satisfied, we solve the usual differential equation for T_χ [Eq. (18)].
 - (b) Otherwise, the SDM is tightly coupled to the baryons, and we can use $\bar{T}_{\chi b}$ and $\Delta T_{b\chi}$ that we obtained in item 1 to find T_χ via $T_\chi = \bar{T}_{\chi b} - \Delta T_{b\chi}/2$.

For the threshold of the DM-TCA small parameter we use $\epsilon_{\chi b}^{\text{th}} = \epsilon_{\gamma b}^{\text{th}} = 5 \times 10^{-5}$ at high redshifts ($z > 100$) and $\epsilon_{\chi b}^{\text{th}} = 10^{-2}$ at low redshifts. We have confirmed that the results of our code are insensitive to these particular values. Moreover, we have confirmed the correctness of our solutions to T_b and T_χ by comparing them to the solutions that can be obtained by solving Eqs. (17)–(20) with *Mathematica* [170] (when all the fluctuations in the box are turned off and we set $L_\chi = 35$, namely no x-ray heating). Unlike our code, *Mathematica* solves differential equations by adjusting the step size so that the estimated error in the solution is just within the specified absolute and relative tolerances. In fact, our DM-TCA algorithm presented above allows one to correctly solve the differential equations even for cross sections that are large enough such that the normal settings in *Mathematica* fail to solve the equations.

APPENDIX D: SMALL TEMPERATURE CORRECTION FOR S_α

The Ly α coupling in Eq. (2) is given by [162]

$$\tilde{x}_\alpha = \frac{J_\alpha}{J_0} \tilde{S}_\alpha, \quad (\text{D1})$$

where J_α is the Ly α flux, and J_0 is

$$\begin{aligned} J_0 &= \frac{9A_{10}T_\gamma}{8\pi\lambda_{\text{Ly}\alpha}^2\gamma_\alpha T_\star} \\ &= 5.54 \times 10^{-12} (1+z) \text{ cm}^{-2} \text{ sec}^{-1} \text{ Hz}^{-1} \text{ sr}^{-1}, \quad (\text{D2}) \end{aligned}$$

where $\lambda_{\text{Ly}\alpha}^2 = 121.567$ nm is the Ly α frequency, $A_{10} = 2.85 \times 10^{-15}$ sec $^{-1}$ is the spontaneous emission coefficient from the excited hyperfine level to the ground state, and $\gamma_\alpha \approx 50$ MHz is the half width at half maximum of the Ly α resonance line.

The quantity \tilde{S}_α that appears in Eq. (D1) is a correction to \bar{x}_α due to spectral distortions. In order to find it, one must solve the steady-state Fokker-Planck equation. This was first numerically solved by Chen and Miralde-Escudé [131] and later was refined by Hirata [128], who found a complicated fit for \tilde{S}_α that depends on T_k , T_s and the Gunn-Peterson optical depth τ_{GP} . In addition, Hirata found a fit for the color temperature, $T_\alpha^{-1} = T_k^{-1} + T_{\text{se}} T_k^{-1} (T_s^{-1} - T_k^{-1})$, where T_{se} accounts for the correction in the color temperature due to spin exchange and is given by

$$T_{\text{se}} = \left(\frac{\lambda_{\text{Ly}\alpha}}{\lambda_{21}} \right)^2 \frac{m_{\text{H}} c^2}{9k_B} \approx 0.4 \text{ K}, \quad (\text{D3})$$

where $\lambda_{21} \approx 21$ cm is the wavelength of a 21-cm photon. The fits discovered by Hirata are implemented in 21cmFAST.

Shortly after Hirata's work, Chuzhoy and Shapiro [161] found an analytical solution to the steady-state Fokker-Planck equation by approximating the spectrum with the absorption profile appropriate to Lorentzian wings (this was first done by Grachev [171]). This is known as the wing approximation. Based on their work, Furlanetto and Pritchard [172] gave analytical estimates, including for the color temperature,

$$T_\alpha = T_s \frac{T_k + T_{\text{se}}}{T_s + T_{\text{se}}}. \quad (\text{D4})$$

Note that in the limit $T_{\text{se}} \ll T_k, T_s$ Eq. (D4) converges to Hirata's fit. Recently, Ref. [162] used the results of Furlanetto and Pritchard to write the analytical estimate for \tilde{S}_α in the following way:

$$\tilde{S}_\alpha(\xi) = 1 - \int_0^\infty e^{-\xi(u/3)^3} e^{-u} du = \begin{cases} 1 & \xi \rightarrow \infty \\ \frac{2}{9}\xi & \xi \ll 1 \end{cases}, \quad (\text{D5})$$

where

$$\begin{aligned} \xi &\equiv \frac{3\nu_{\text{Ly}\alpha} m_{\text{H}} H(k_B T_k)^2}{\pi A_\alpha \gamma_\alpha c \hbar^3 n_{\text{H}} (1 - x_e)} \\ &\approx 760 \left(\frac{\Omega_m h^2}{0.143} \right)^{1/2} \left(\frac{\Omega_b h^2}{0.0223} \right)^{-1} \left(\frac{1 - Y_{\text{He}}}{0.755} \right)^{-1} \\ &\quad \times \left(\frac{T_k}{10 \text{ K}} \right)^2 \left(\frac{1+z}{15} \right)^{-3/2} \frac{1}{(1 + \delta_b)(1 - x_e)}, \end{aligned} \quad (\text{D6})$$

where $\nu_{\text{Ly}\alpha} = 2.47 \times 10^{15}$ Hz is the Ly α frequency and $A_\alpha = 6.25 \times 10^8$ Hz is the spontaneous Ly α emission coefficient. The fiducial values in Eq. (D6) correspond

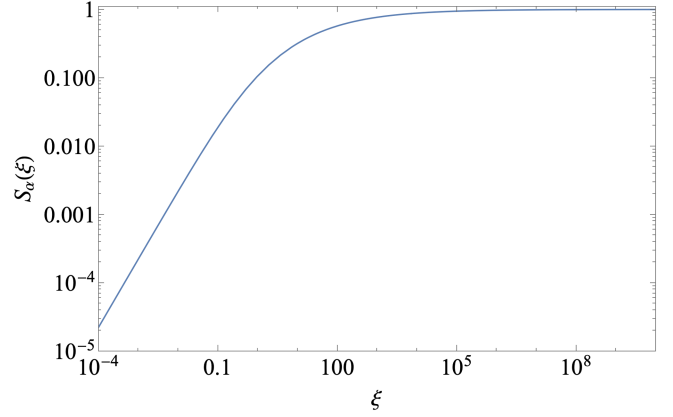


FIG. 18. The function $\tilde{S}_\alpha(\xi)$ as given by Eq. (D5).

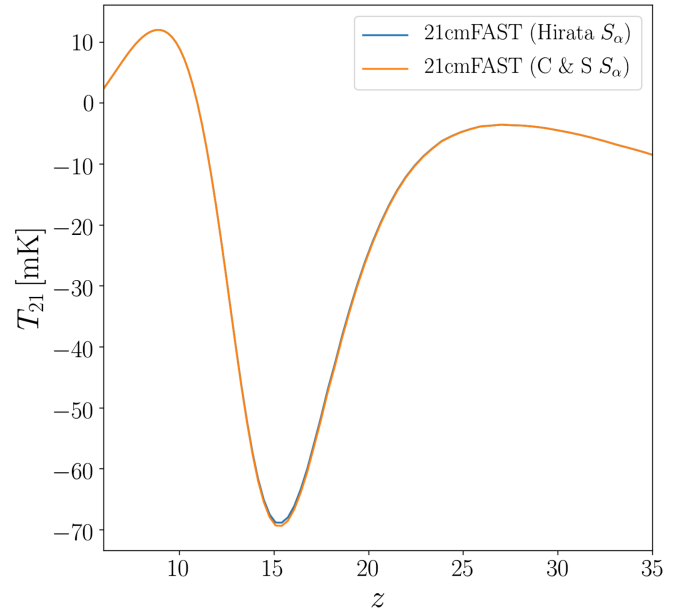


FIG. 19. Comparison of the 21cm global signal when \tilde{S}_α is calculated from Ref. [128] (Hirata) or Ref. [161] (Chuzhoy and Shapiro). In both curves early temperature and ionization fluctuations were discarded by starting the simulation at $z = 35$.

to typical values of T_k at $z = 15$ in Λ CDM (cf. Fig. 1). According to Fig. 18, $\xi \sim 10^3$ corresponds to $\tilde{S}_\alpha \sim 0.5$.

In SDM however, the gas kinetic temperature may reach very low temperatures (cf. Fig. 9) where Hirata's fit to \tilde{S}_α no longer works. Therefore, for our SDM calculations in this paper we follow¹⁸ [107] and work with Eqs. (D4)–(D6). In Figs. 19 and 20 we verify that in Λ CDM

¹⁸It is worth mentioning that another fit for \tilde{S}_α at low temperature exists in the literature [124,173]. However, implementing this fit in 21cmFirstCLASS did not yield results that agree with either [128] or [161].

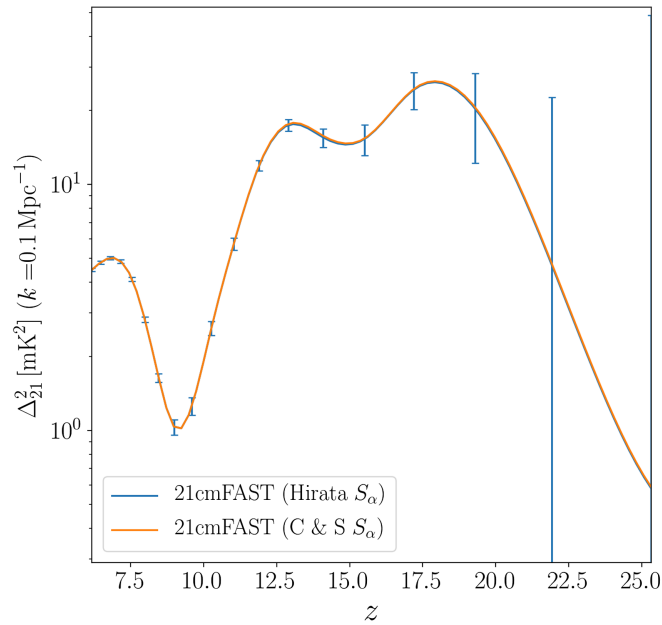


FIG. 20. Comparison of the 21-cm power spectrum when \tilde{S}_α is calculated from Ref. [128] (Hirata) or Ref. [161] (Chuzhoy and Shapiro). In both curves early temperature and ionization fluctuations were discarded by starting the simulation at $z = 35$. Optimistic foreground scenario is assumed for the error bars.

the output of our code is not sensitive to the chosen method. Indeed, there is an excellent agreement between the two methods.

Because $\xi \propto T_k^2$ and T_k can be smaller by a factor of $\sim 10^2$ compared to Λ CDM, the value of ξ may drop below 0.1, and from Fig. 18 it is implied that $\tilde{S}_\alpha < 0.01$. This explains why in Fig. 9, T_s cannot reach very low temperatures even though T_k does.

-
- [1] S. M. Carroll, The cosmological constant, *Living Rev. Relativity* **4**, 1 (2001).
 - [2] P. J. E. Peebles, Tests of cosmological models constrained by inflation, *Astrophys. J.* **284**, 439 (1984).
 - [3] P. J. E. Peebles and B. Ratra, The cosmological constant and dark energy, *Rev. Mod. Phys.* **75**, 559 (2003).
 - [4] P. Bull *et al.*, Beyond Λ CDM: Problems, solutions, and the road ahead, *Phys. Dark Universe* **12**, 56 (2016).
 - [5] Y. Wang and G.-B. Zhao, A brief review on cosmological analysis of galaxy surveys with multiple tracers, *Res. Astron. Astrophys.* **20**, 158 (2020).
 - [6] C. Zhao *et al.*, The completed SDSS-IV extended Baryon Oscillation Spectroscopic Survey: Cosmological implications from multitracer BAO analysis with galaxies and voids, *Mon. Not. R. Astron. Soc.* **511**, 5492 (2022).
 - [7] A. G. Sanchez *et al.* (BOSS Collaboration), The clustering of galaxies in the completed SDSS-III Baryon Oscillation Spectroscopic Survey: Cosmological implications of the configuration-space clustering wedges, *Mon. Not. R. Astron. Soc.* **464**, 1640 (2017).
 - [8] J. N. Grieb *et al.* (BOSS Collaboration), The clustering of galaxies in the completed SDSS-III Baryon Oscillation Spectroscopic Survey: Cosmological implications of the Fourier space wedges of the final sample, *Mon. Not. R. Astron. Soc.* **467**, 2085 (2017).
 - [9] S. Alam *et al.* (eBOSS Collaboration), Completed SDSS-IV extended Baryon Oscillation Spectroscopic Survey: Cosmological implications from two decades of spectroscopic surveys at the Apache Point Observatory, *Phys. Rev. D* **103**, 083533 (2021).
 - [10] W. J. Percival *et al.* (2dFGRS Team), Parameter constraints for flat cosmologies from CMB and 2dFGRS power spectra, *Mon. Not. R. Astron. Soc.* **337**, 1068 (2002).
 - [11] C. Blake *et al.*, The WiggleZ dark energy survey: Testing the cosmological model with baryon acoustic oscillations at $z = 0.6$, *Mon. Not. R. Astron. Soc.* **415**, 2892 (2011).
 - [12] A. Johnson *et al.*, The 6dF galaxy survey: Cosmological constraints from the velocity power spectrum, *Mon. Not. R. Astron. Soc.* **444**, 3926 (2014).
 - [13] E. van Uitert *et al.*, KiDS + GAMA: Cosmology constraints from a joint analysis of cosmic shear,

- galaxy–galaxy lensing, and angular clustering, *Mon. Not. R. Astron. Soc.* **476**, 4662 (2018).
- [14] R. Chen *et al.* (DES Collaboration), Measuring cosmological parameters with type Ia supernovae in redMaGiC galaxies, *Astrophys. J.* **938**, 62 (2022).
- [15] C. Doux *et al.* (DES Collaboration), Dark Energy Survey Year 3 results: Cosmological constraints from the analysis of cosmic shear in harmonic space, *Mon. Not. R. Astron. Soc.* **515**, 1942 (2022).
- [16] M. Gatti *et al.* (DES Collaboration), Dark Energy Survey Year 3 results: Cosmology with moments of weak lensing mass maps, *Phys. Rev. D* **106**, 083509 (2022).
- [17] A. Porredon *et al.* (DES Collaboration), Dark Energy Survey Year 3 results: Cosmological constraints from galaxy clustering and galaxy-galaxy lensing using the MagLim lens sample, *Phys. Rev. D* **106**, 103530 (2022).
- [18] T. M. C. Abbott *et al.* (DES Collaboration), Dark Energy Survey Year 3 results: Cosmological constraints from galaxy clustering and weak lensing, *Phys. Rev. D* **105**, 023520 (2022).
- [19] M. Costanzi *et al.* (DES, SPT Collaborations), Cosmological constraints from DES Y1 cluster abundances and SPT multiwavelength data, *Phys. Rev. D* **103**, 043522 (2021).
- [20] C. To *et al.* (DES Collaboration), Dark Energy Survey Year 1 results: Cosmological constraints from cluster abundances, weak lensing, and galaxy correlations, *Phys. Rev. Lett.* **126**, 141301 (2021).
- [21] R. A. C. Croft, D. H. Weinberg, N. Katz, and L. Hernquist, Recovery of the power spectrum of mass fluctuations from observations of the Ly α forest, *Astrophys. J.* **495**, 44 (1998).
- [22] P. McDonald, J. Miralda-Escude, M. Rauch, W. L. W. Sargent, T. A. Barlow, R. Cen, and J. P. Ostriker, The observed probability distribution function, power spectrum, and correlation function of the transmitted flux in the Lyman-alpha forest, *Astrophys. J.* **543**, 1 (2000).
- [23] P. McDonald *et al.* (SDSS Collaboration), The linear theory power spectrum from the Ly α forest in the Sloan Digital Sky Survey, *Astrophys. J.* **635**, 761 (2005).
- [24] M. Viel, M. G. Haehnelt, and V. Springel, Inferring the dark matter power spectrum from the Lyman α forest in high-resolution QSO absorption spectra, *Mon. Not. R. Astron. Soc.* **354**, 684 (2004).
- [25] P. McDonald *et al.* (SDSS Collaboration), The Ly α forest power spectrum from the Sloan Digital Sky Survey, *Astrophys. J. Suppl. Ser.* **163**, 80 (2006).
- [26] S. Dodelson, *Modern Cosmology* (Academic Press, Amsterdam, 2003).
- [27] J. Lesgourgues, Cosmological perturbations, in *Theoretical Advanced Study Institute in Elementary Particle Physics: Searching for New Physics at Small and Large Scales* (World Scientific, 2013), pp. 29–97, [arXiv:1302.4640](https://arxiv.org/abs/1302.4640).
- [28] W. Hu, Concepts in CMB anisotropy formation, *Lect. Notes Phys.* **470**, 207 (1996).
- [29] A. Challinor and H. Peiris, Lecture notes on the physics of cosmic microwave background anisotropies, *AIP Conf. Proc.* **1132**, 86 (2009).
- [30] W. Hu, Lecture notes on CMB theory: From nucleosynthesis to recombination, [arXiv:0802.3688](https://arxiv.org/abs/0802.3688).
- [31] W. T. Hu, Wandering in the background: A CMB explorer, Other thesis, University of California, 1995.
- [32] W. Hu and M. J. White, A CMB polarization primer, *New Astron.* **2**, 323 (1997).
- [33] A. Kosowsky, Introduction to microwave background polarization, *New Astron. Rev.* **43**, 157 (1999).
- [34] P. Cabella and M. Kamionkowski, Theory of cosmic microwave background polarization, in *International School of Gravitation and Cosmology: The Polarization of the Cosmic Microwave Background* (2004), [arXiv:astro-ph/0403392](https://arxiv.org/abs/astro-ph/0403392).
- [35] Y.-T. Lin and B. D. Wandelt, A beginner’s guide to the theory of CMB temperature and polarization power spectra in the line-of-sight formalism, *Astropart. Phys.* **25**, 151 (2006).
- [36] A. Lewis and A. Challinor, Weak gravitational lensing of the CMB, *Phys. Rep.* **429**, 1 (2006).
- [37] N. Aghanim *et al.* (Planck Collaboration), Planck 2018 results. I. Overview and the cosmological legacy of Planck, *Astron. Astrophys.* **641**, A1 (2020).
- [38] L. Balkenhol *et al.* (SPT-3G Collaboration), Measurement of the CMB temperature power spectrum and constraints on cosmology from the SPT-3G 2018 TT, TE, and EE dataset, *Phys. Rev. D* **108**, 023510 (2023).
- [39] G. A. Marques *et al.* (ACT, DES Collaborations), Cosmological constraints from the tomography of DES-Y3 galaxies with CMB lensing from ACT DR4, [arXiv:2306.17268](https://arxiv.org/abs/2306.17268).
- [40] N. Aghanim *et al.* (Planck Collaboration), Planck 2018 results. VI. Cosmological parameters, *Astron. Astrophys.* **641**, A6 (2020); **652**, C4(E) (2021).
- [41] J. S. Bullock and M. Boylan-Kolchin, Small-scale challenges to the Λ CDM paradigm, *Annu. Rev. Astron. Astrophys.* **55**, 343 (2017).
- [42] L. Perivolaropoulos and F. Skara, Challenges for Λ CDM: An update, *New Astron. Rev.* **95**, 101659 (2022).
- [43] M. Kamionkowski and A. G. Riess, The Hubble tension and early dark energy, *Annu. Rev. Nucl. Part. Sci.* **73**, 153 (2023).
- [44] E. Abdalla *et al.*, Cosmology intertwined: A review of the particle physics, astrophysics, and cosmology associated with the cosmological tensions and anomalies, *J. High Energy Astrophys.* **34**, 49 (2022).
- [45] R. H. Cyburt, B. D. Fields, K. A. Olive, and T.-H. Yeh, Big bang nucleosynthesis: 2015, *Rev. Mod. Phys.* **88**, 015004 (2016).
- [46] C. Pitrou, A. Coc, J.-P. Uzan, and E. Vangioni, Precision big bang nucleosynthesis with improved Helium-4 predictions, *Phys. Rep.* **754**, 1 (2018).
- [47] P. Madau, A. Meiksin, and M. J. Rees, 21-cm tomography of the intergalactic medium at high redshift, *Astrophys. J.* **475**, 429 (1997).
- [48] R. Barkana and A. Loeb, In the beginning: The first sources of light and the reionization of the universe, *Phys. Rep.* **349**, 125 (2001).
- [49] A. Loeb and M. Zaldarriaga, Measuring the small-scale power spectrum of cosmic density fluctuations through 21cm tomography prior to the epoch of structure formation, *Phys. Rev. Lett.* **92**, 211301 (2004).
- [50] S. Bharadwaj and S. S. Ali, On using visibility correlations to probe the HI distribution from the dark ages to the

- present epoch. I. Formalism and the expected signal, *Mon. Not. R. Astron. Soc.* **356**, 1519 (2005).
- [51] S. Furlanetto, S. P. Oh, and F. Briggs, Cosmology at low frequencies: The 21cm transition and the high-redshift universe, *Phys. Rep.* **433**, 181 (2006).
- [52] J. R. Pritchard and A. Loeb, 21-cm cosmology, *Rep. Prog. Phys.* **75**, 086901 (2012).
- [53] A. Bera, R. Ghara, A. Chatterjee, K. K. Datta, and S. Samui, Studying cosmic dawn using redshifted HI 21-cm signal: A brief review, *J. Astrophys. Astron.* **44**, 10 (2023).
- [54] A. K. Shaw *et al.*, Probing early Universe through redshifted 21-cm signal: Modeling and observational challenges, *J. Astrophys. Astron.* **44**, 4 (2023).
- [55] R. A. Monsalve, A. Fialkov, J. D. Bowman, A. E. E. Rogers, T. J. Mozdzen, A. Cohen, R. Barkana, and N. Mahesh, Results from EDGES high-band: III. New Constraints on parameters of the early universe, *Astrophys. J.* **875**, 67 (2019).
- [56] J. Nambissan, R. Subrahmanyam, R. Somashekar, N. Udaya Shankar, S. Singh, A. Raghunathan, B. S. Girish, K. S. Srivani, and M. Sathyanarayana Rao, SARAS 3 CD/EoR radiometer: Design and performance of the receiver, *Exp. Astron.* **51**, 193 (2021).
- [57] D. C. Price *et al.*, Design and characterization of the large-aperture experiment to detect the dark age (LEDA) radiometer systems, *Mon. Not. R. Astron. Soc.* **478**, 4193 (2018).
- [58] E. de Lera Acedo *et al.*, The REACH radiometer for detecting the 21-cm hydrogen signal from redshift $z \approx 7.5$ –28, *Nat. Astron.* **6**, 998 (2022).
- [59] L. Philip, Z. Abdurashidova, H. C. Chiang, N. Ghazi, A. Gumba, H. M. Heilgendorff, J. M. Jáuregui-García, K. Malepe, C. D. Nunhokee, J. Peterson, J. L. Sievers, V. Simes, and R. Spann, Probing radio intensity at high- Z from Marion: 2017 instrument, *J. Astron. Instrum.* **8**, 1950004 (2019).
- [60] S. Pal, S. Bharadwaj, A. Ghosh, and S. Choudhuri, Demonstrating the Tapered Gridded Estimator (TGE) for the cosmological H I 21-cm power spectrum using 150-MHz GMRT observations, *Mon. Not. R. Astron. Soc.* **501**, 3378 (2021).
- [61] S. Yoshiura *et al.*, A new MWA limit on the 21cm power spectrum at redshifts ~ 13 –17, *Mon. Not. R. Astron. Soc.* **505**, 4775 (2021).
- [62] F. G. Mertens *et al.*, Improved upper limits on the 21-cm signal power spectrum of neutral hydrogen at $z \approx 9.1$ from LOFAR, *Mon. Not. R. Astron. Soc.* **493**, 1662 (2020).
- [63] A. R. Parsons *et al.*, New limits on 21cm EoR from PAPER-32 consistent with an x-ray heated IGM at $z = 7.7$, *Astrophys. J.* **788**, 106 (2014).
- [64] D. R. DeBoer *et al.*, Hydrogen Epoch of Reionization Array (HERA), *Publ. Astron. Soc. Pac.* **129**, 045001 (2017).
- [65] R. Braun, T. Bourke, J. A. Green, E. Keane, and J. Wagg, Advancing astrophysics with the square kilometre array, *Proc. Sci. AASKA14* (2015) 174.
- [66] Z. Abdurashidova *et al.* (HERA Collaboration), HERA phase I limits on the cosmic 21cm signal: Constraints on astrophysics and cosmology during the epoch of reionization, *Astrophys. J.* **924**, 51 (2022).
- [67] Z. Abdurashidova *et al.* (HERA Collaboration), First results from HERA phase I: Upper limits on the epoch of reionization 21cm power spectrum, *Astrophys. J.* **925**, 221 (2022).
- [68] Z. Abdurashidova *et al.* (HERA Collaboration), Improved constraints on the 21cm EoR power spectrum and the x-ray heating of the IGM with HERA phase I observations, *Astrophys. J.* **945**, 124 (2023).
- [69] H. Lazare, D. Sarkar, and E. D. Kovetz, HERA bound on x-ray luminosity weakens when accounting for Population III stars, *arXiv:2307.15577*.
- [70] P. Ocvirk *et al.*, Cosmic Dawn (CoDA): The first radiation-hydrodynamics simulation of reionization and galaxy formation in the local universe, *Mon. Not. R. Astron. Soc.* **463**, 1462 (2016).
- [71] P. Ocvirk *et al.*, Cosmic Dawn II (CoDA II): A new radiation-hydrodynamics simulation of the self-consistent coupling of galaxy formation and reionization, *Mon. Not. R. Astron. Soc.* **496**, 4087 (2020).
- [72] J. S. W. Lewis *et al.*, The short ionizing photon mean free path at $z = 6$ in Cosmic Dawn III, a new fully coupled radiation-hydrodynamical simulation of the epoch of reionization, *Mon. Not. R. Astron. Soc.* **516**, 3389 (2022).
- [73] B. Semelin, E. Eames, F. Bolgar, and M. Caillat, 21SSD: A public data base of simulated 21-cm signals from the epoch of reionization, *Mon. Not. R. Astron. Soc.* **472**, 4508 (2017).
- [74] R. Kannan, E. Garaldi, A. Smith, R. Pakmor, V. Springel, M. Vogelsberger, and L. Hernquist, Introducing the THESAN project: Radiation-magnetohydrodynamic simulations of the epoch of reionization, *Mon. Not. R. Astron. Soc.* **511**, 4005 (2022).
- [75] G. Mellema, I. Iliev, M. Alvarez, and P. Shapiro, C^2 -ray: A new method for photon-conserving transport of ionizing radiation, *New Astron.* **11**, 374 (2006).
- [76] A. Maselli, A. Ferrara, and B. Ciardi, CRASH: A radiative transfer scheme, *Mon. Not. R. Astron. Soc.* **345**, 379 (2003).
- [77] R. M. Thomas *et al.*, Fast large-scale reionization simulations, *Mon. Not. R. Astron. Soc.* **393**, 32 (2009).
- [78] R. Ghara, G. Mellema, S. K. Giri, T. R. Choudhury, K. K. Datta, and S. Majumdar, Prediction of the 21-cm signal from reionization: Comparison between 3D and 1D radiative transfer schemes, *Mon. Not. R. Astron. Soc.* **476**, 1741 (2018).
- [79] T. Schaeffer, S. K. Giri, and A. Schneider, BEORN: A fast and flexible framework to simulate the epoch of reionisation and cosmic dawn, *arXiv:2305.15466*.
- [80] A. Schneider, S. K. Giri, and J. Mirocha, Halo model approach for the 21-cm power spectrum at cosmic dawn, *Phys. Rev. D* **103**, 083025 (2021).
- [81] J. B. Muñoz, An effective model for the cosmic-dawn 21-cm signal, *Mon. Not. R. Astron. Soc.* **523**, 2587 (2023).
- [82] S. Furlanetto, M. Zaldarriaga, and L. Hernquist, Statistical probes of reionization with 21cm tomography, *Astrophys. J.* **613**, 16 (2004).
- [83] I. Reis, A. Fialkov, and R. Barkana, The subtlety of Ly α photons: Changing the expected range of the 21-cm signal, *Mon. Not. R. Astron. Soc.* **506**, 5479 (2021).

- [84] M. Santos, L. Ferramacho, M. Silva, A. Amblard, and A. Cooray, *SimFast21*: Simulation of the cosmological 21cm signal, Astrophysics Source Code Library, record ascl:1010.025 (2010).
- [85] A. Mesinger, S. Furlanetto, and R. Cen, 21cmFAST: A fast, semi-numerical simulation of the high-redshift 21-cm signal, *Mon. Not. R. Astron. Soc.* **411**, 955 (2011).
- [86] J. B. Muñoz, Y. Qin, A. Mesinger, S. G. Murray, B. Greig, and C. Mason, The impact of the first galaxies on cosmic dawn and reionization, *Mon. Not. R. Astron. Soc.* **511**, 3657 (2022).
- [87] D. Blas, J. Lesgourgues, and T. Tram, The Cosmic Linear Anisotropy Solving System (CLASS) II: Approximation schemes, *J. Cosmol. Astropart. Phys.* **07** (2011) 034.
- [88] Z. Haiman, M. J. Rees, and A. Loeb, Destruction of molecular hydrogen during cosmological reionization, *Astrophys. J.* **476**, 458 (1997).
- [89] V. Bromm and R. B. Larson, The first stars, *Annu. Rev. Astron. Astrophys.* **42**, 79 (2004).
- [90] A. Fialkov, R. Barkana, E. Visbal, D. Tseliakhovich, and C. M. Hirata, The 21-cm signature of the first stars during the Lyman-Werner feedback era, *Mon. Not. R. Astron. Soc.* **432**, 2909 (2013).
- [91] D. Tseliakhovich and C. Hirata, Relative velocity of dark matter and baryonic fluids and the formation of the first structures, *Phys. Rev. D* **82**, 083520 (2010).
- [92] D. Tseliakhovich, R. Barkana, and C. Hirata, Suppression and spatial variation of early galaxies and minihalos, *Mon. Not. R. Astron. Soc.* **418**, 906 (2011).
- [93] A. Fialkov, R. Barkana, D. Tseliakhovich, and C. M. Hirata, Impact of the relative motion between the dark matter and baryons on the first stars, *Mon. Not. R. Astron. Soc.* **424**, 1335 (2012).
- [94] Y. Ali-Haïmoud, P. D. Meerburg, and S. Yuan, New light on 21cm intensity fluctuations from the dark ages, *Phys. Rev. D* **89**, 083506 (2014).
- [95] T. Venumadhav, L. Dai, A. Kaurov, and M. Zaldarriaga, Heating of the intergalactic medium by the cosmic microwave background during cosmic dawn, *Phys. Rev. D* **98**, 103513 (2018).
- [96] D. Sarkar, J. Flitter, and E. D. Kovetz, Exploring delaying and heating effects on the 21-cm signature of fuzzy dark matter, *Phys. Rev. D* **105**, 103529 (2022).
- [97] J. Flitter and E. D. Kovetz, Closing the window on fuzzy dark matter with the 21-cm signal, *Phys. Rev. D* **106**, 063504 (2022).
- [98] H. A. G. Cruz, T. Adi, J. Flitter, M. Kamionkowski, and E. D. Kovetz, 21-cm fluctuations from primordial magnetic fields, [arXiv:2308.04483](https://arxiv.org/abs/2308.04483).
- [99] C. Dvorkin, K. Blum, and M. Kamionkowski, Constraining dark matter-baryon scattering with linear cosmology, *Phys. Rev. D* **89**, 023519 (2014).
- [100] J. B. Muñoz, E. D. Kovetz, and Y. Ali-Haïmoud, Heating of baryons due to scattering with dark matter during the dark ages, *Phys. Rev. D* **92**, 083528 (2015).
- [101] K. K. Boddy, V. Gluscevic, V. Poulin, E. D. Kovetz, M. Kamionkowski, and R. Barkana, Critical assessment of CMB limits on dark matter-baryon scattering: New treatment of the relative bulk velocity, *Phys. Rev. D* **98**, 123506 (2018).
- [102] A. Fialkov, R. Barkana, and A. Cohen, Constraining baryon–dark matter scattering with the cosmic dawn 21-cm signal, *Phys. Rev. Lett.* **121**, 011101 (2018).
- [103] W. L. Xu, C. Dvorkin, and A. Chael, Probing sub-GeV dark matter-baryon scattering with cosmological observables, *Phys. Rev. D* **97**, 103530 (2018).
- [104] R. Barkana, Possible interaction between baryons and dark-matter particles revealed by the first stars, *Nature (London)* **555**, 71 (2018).
- [105] K. Short, J. L. Bernal, K. K. Boddy, V. Gluscevic, and L. Verde, Dark matter-baryon scattering effects on temperature perturbations and implications for cosmic dawn, [arXiv:2203.16524](https://arxiv.org/abs/2203.16524).
- [106] A. He, M. M. Ivanov, R. An, and V. Gluscevic, S_8 tension in the context of dark matter-baryon scattering, *Astrophys. J. Lett.* **954**, L8 (2023).
- [107] T. Driskell, E. O. Nadler, J. Mirocha, A. Benson, K. K. Boddy, T. D. Morton, J. Lashner, R. An, and V. Gluscevic, Structure formation and the global 21-cm signal in the presence of Coulomb-like dark matter-baryon interactions, *Phys. Rev. D* **106**, 103525 (2022).
- [108] S. D. McDermott, H.-B. Yu, and K. M. Zurek, Turning off the lights: How dark is dark matter?, *Phys. Rev. D* **83**, 063509 (2011).
- [109] E. D. Kovetz, V. Poulin, V. Gluscevic, K. K. Boddy, R. Barkana, and M. Kamionkowski, Tighter limits on dark matter explanations of the anomalous EDGES 21cm signal, *Phys. Rev. D* **98**, 103529 (2018).
- [110] J. B. Muñoz and A. Loeb, A small amount of mini-charged dark matter could cool the baryons in the early universe, *Nature (London)* **557**, 684 (2018).
- [111] A. Berlin, D. Hooper, G. Krnjaic, and S. D. McDermott, Severely constraining dark matter interpretations of the 21-cm anomaly, *Phys. Rev. Lett.* **121**, 011102 (2018).
- [112] R. Barkana, N. J. Outmezguine, D. Redigolo, and T. Volansky, Strong constraints on light dark matter interpretation of the EDGES signal, *Phys. Rev. D* **98**, 103005 (2018).
- [113] T. R. Slatyer and C.-L. Wu, Early-universe constraints on dark matter-baryon scattering and their implications for a global 21cm signal, *Phys. Rev. D* **98**, 023013 (2018).
- [114] H. Liu and T. R. Slatyer, Implications of a 21-cm signal for dark matter annihilation and decay, *Phys. Rev. D* **98**, 023501 (2018).
- [115] J. B. Muñoz, C. Dvorkin, and A. Loeb, 21-cm fluctuations from charged dark matter, *Phys. Rev. Lett.* **121**, 121301 (2018).
- [116] Y. Ali-Haïmoud, J. Chluba, and M. Kamionkowski, Constraints on dark matter interactions with standard model particles from cosmic microwave background spectral distortions, *Phys. Rev. Lett.* **115**, 071304 (2015).
- [117] V. Gluscevic and K. K. Boddy, Constraints on scattering of keV–TeV dark matter with protons in the early universe, *Phys. Rev. Lett.* **121**, 081301 (2018).
- [118] K. K. Boddy and V. Gluscevic, First cosmological constraint on the effective theory of dark matter-proton interactions, *Phys. Rev. D* **98**, 083510 (2018).
- [119] K. Maamari, V. Gluscevic, K. K. Boddy, E. O. Nadler, and R. H. Wechsler, Bounds on velocity-dependent dark

- matter-proton scattering from Milky Way satellite abundance, *Astrophys. J. Lett.* **907**, L46 (2021).
- [120] D. V. Nguyen, D. Sarnaik, K. K. Boddy, E. O. Nadler, and V. Gluscevic, Observational constraints on dark matter scattering with electrons, *Phys. Rev. D* **104**, 103521 (2021).
- [121] M. A. Buen-Abad, R. Essig, D. McKeen, and Y.-M. Zhong, Cosmological constraints on dark matter interactions with ordinary matter, *Phys. Rep.* **961**, 1 (2022).
- [122] K. K. Rogers, C. Dvorkin, and H. V. Peiris, Limits on the light dark matter–proton cross section from cosmic large-scale structure, *Phys. Rev. Lett.* **128**, 171301 (2022).
- [123] H. Liu, N. J. Outmezguine, D. Redigolo, and T. Volansky, Reviving millicharged dark matter for 21-cm cosmology, *Phys. Rev. D* **100**, 123011 (2019).
- [124] R. Barkana, A. Fialkov, H. Liu, and N. J. Outmezguine, Anticipating a new-physics signal in upcoming 21-cm power spectrum observations, *Phys. Rev. D* **108**, 063503 (2023).
- [125] J. Mirocha, Decoding the x-ray properties of pre-reionization era sources, *Mon. Not. R. Astron. Soc.* **443**, 1211 (2014).
- [126] J. Mirocha, S. R. Furlanetto, and G. Sun, The global 21-cm signal in the context of the high- z galaxy luminosity function, *Mon. Not. R. Astron. Soc.* **464**, 1365 (2017).
- [127] J. Flitter and E. D. Kovetz, following paper, New tool for 21-cm cosmology. II. Investigating the effect of early linear fluctuations, *Phys. Rev. D* **109**, 043513 (2024).
- [128] C. M. Hirata, Wouthuysen-Field coupling strength and application to high-redshift 21cm radiation, *Mon. Not. R. Astron. Soc.* **367**, 259 (2006).
- [129] S. A. Wouthuysen, On the excitation mechanism of the 21-cm (radio-frequency) interstellar hydrogen emission line, *Astrophys. J.* **57**, 31 (1952).
- [130] G. B. Field, Excitation of the hydrogen 21-CM line, *Proc. IRE* **46**, 240 (1958).
- [131] X.-L. Chen and J. Miralda-Escude, The spin—kinetic temperature coupling and the heating rate due to Ly α scattering before reionization: Predictions for 21cm emission and absorption, *Astrophys. J.* **602**, 1 (2004).
- [132] Y. Ali-Haïmoud and C. M. Hirata, HyRec: A fast and highly accurate primordial hydrogen and helium recombination code, *Phys. Rev. D* **83**, 043513 (2011).
- [133] N. Lee and Y. Ali-Haïmoud, HyRec-2: A highly accurate sub-millisecond recombination code, *Phys. Rev. D* **102**, 083517 (2020).
- [134] P. J. E. Peebles, Recombination of the primeval plasma, *Astrophys. J.* **153**, 1 (1968).
- [135] T. Abel, P. Anninos, Y. Zhang, and M. L. Norman, Modeling primordial gas in numerical cosmology, *New Astron.* **2**, 181 (1997).
- [136] Y. Mao, J. Koda, P. R. Shapiro, I. T. Iliev, G. Mellema, H. Park, K. Ahn, and M. Bianco, The impact of inhomogeneous subgrid clumping on cosmic reionization, *Mon. Not. R. Astron. Soc.* **491**, 1600 (2020).
- [137] A. R. Liddle, D. H. Lyth, P. T. P. Viana, and M. J. White, Cold dark matter models with a cosmological constant, *Mon. Not. R. Astron. Soc.* **282**, 281 (1996).
- [138] S. M. Carroll, W. H. Press, and E. L. Turner, The cosmological constant, *Annu. Rev. Astron. Astrophys.* **30**, 499 (1992).
- [139] S. Seager, D. D. Sasselov, and D. Scott, A new calculation of the recombination epoch, *Astrophys. J. Lett.* **523**, L1 (1999).
- [140] S. Seager, D. D. Sasselov, and D. Scott, How exactly did the universe become neutral?, *Astrophys. J. Suppl. Ser.* **128**, 407 (2000).
- [141] S. G. Murray, POWERBOX: A Python package for creating structured fields with isotropic power spectra, *J. Open Source Software* **3**, 850 (2018).
- [142] G. Jungman, M. Kamionkowski, A. Kosowsky, and D. N. Spergel, Cosmological parameter determination with microwave background maps, *Phys. Rev. D* **54**, 1332 (1996).
- [143] C. A. Mason, J. B. Muñoz, B. Greig, A. Mesinger, and J. Park, 21cm fish: Fisher-matrix framework for fast parameter forecasts from the cosmic 21-cm signal, *Mon. Not. R. Astron. Soc.* **524**, 4711 (2022).
- [144] N. S. Kern, A. Liu, A. R. Parsons, A. Mesinger, and B. Greig, Emulating simulations of cosmic dawn for 21cm power spectrum constraints on cosmology, reionization, and x-ray heating, *Astrophys. J.* **848**, 23 (2017).
- [145] G. Shmueli, D. Sarkar, and E. D. Kovetz, Mitigating the optical depth degeneracy in the cosmological measurement of neutrino masses using 21-cm observations, *Phys. Rev. D* **108**, 083531 (2023).
- [146] J. C. Pober, A. R. Parsons, D. R. DeBoer, P. McDonald, M. McQuinn, J. E. Aguirre, Z. Ali, R. F. Bradley, T.-C. Chang, and M. F. Morales, The Baryon Acoustic Oscillation broadband and broad-beam array: Design overview and sensitivity forecasts, *Astron. J.* **145**, 65 (2013).
- [147] J. C. Pober *et al.*, What next-generation 21cm power spectrum measurements can teach us about the epoch of reionization, *Astrophys. J.* **782**, 66 (2014).
- [148] A. Liu and J. R. Shaw, Data analysis for precision 21cm cosmology, *Publ. Astron. Soc. Pac.* **132**, 062001 (2020).
- [149] M. F. Morales, B. Hazelton, I. Sullivan, and A. Beardsley, Four fundamental foreground power spectrum shapes for 21cm cosmology observations, *Astrophys. J.* **752**, 137 (2012).
- [150] K. N. Abazajian *et al.* (CMB-S4 Collaboration), CMB-S4 science book, first edition, [arXiv:1610.02743](https://arxiv.org/abs/1610.02743).
- [151] W. L. K. Wu, J. Errard, C. Dvorkin, C. L. Kuo, A. T. Lee, P. McDonald, A. Slosar, and O. Zahn, A guide to designing future ground-based cosmic microwave background experiments, *Astrophys. J.* **788**, 138 (2014).
- [152] J. B. Muñoz, E. D. Kovetz, A. Raccanelli, M. Kamionkowski, and J. Silk, Towards a measurement of the spectral runnings, *J. Cosmol. Astropart. Phys.* **05** (2017) 032.
- [153] T. Adi and E. D. Kovetz, Can conformally coupled modified gravity solve the Hubble tension?, *Phys. Rev. D* **103**, 023530 (2021).
- [154] J. Park, A. Mesinger, B. Greig, and N. Gillet, Inferring the astrophysics of reionization and cosmic dawn from galaxy luminosity functions and the 21-cm signal, *Mon. Not. R. Astron. Soc.* **484**, 933 (2019).
- [155] Y. Qin, A. Mesinger, S. E. I. Bosman, and M. Viel, Reionization and galaxy inference from the high-redshift Ly α forest, *Mon. Not. R. Astron. Soc.* **506**, 2390 (2021).
- [156] J. D. Bowman, A. E. E. Rogers, R. A. Monsalve, T. J. Mozdzen, and N. Mahesh, An absorption profile centred

- at 78 megahertz in the sky-averaged spectrum, *Nature (London)* **555**, 67 (2018).
- [157] S. Singh, Jishnu Nambissan T., R. Subrahmanyam, N. Udaya Shankar, B. S. Girish, A. Raghunathan, R. Somashekar, K. S. Srivani, and M. Sathyanarayana Rao, On the detection of a cosmic dawn signal in the radio background, *Nat. Astron.* **6**, 607 (2022).
- [158] J. B. Muñoz, Robust velocity-induced acoustic oscillations at cosmic dawn, *Phys. Rev. D* **100**, 063538 (2019).
- [159] Y. Ali-Haïmoud, Boltzmann-Fokker-Planck formalism for dark-matter–baryon scattering, *Phys. Rev. D* **99**, 023523 (2019).
- [160] S. S. Gandhi and Y. Ali-Haïmoud, Numerical solution of the exact background collisional Boltzmann equation for dark matter-baryon scattering, *Phys. Rev. D* **106**, 083515 (2022).
- [161] L. Chuzhoy and P. R. Shapiro, UV pumping of hyperfine transitions in the light elements, with application to 21-cm hydrogen and 92-cm deuterium lines from the early universe, *Astrophys. J.* **651**, 1 (2006).
- [162] S. Mittal and G. Kulkarni, Ly α coupling and heating at cosmic dawn, *Mon. Not. R. Astron. Soc.* **503**, 4264 (2021).
- [163] J. B. Muñoz, Standard ruler at cosmic dawn, *Phys. Rev. Lett.* **123**, 131301 (2019).
- [164] D. Sarkar and E. D. Kovetz, Measuring the cosmic expansion rate using 21-cm velocity acoustic oscillations, *Phys. Rev. D* **107**, 023524 (2023).
- [165] M. Kulkarni, E. Visbal, and G. L. Bryan, The critical dark matter halo mass for Population III star formation: Dependence on Lyman–Werner radiation, baryon-dark matter streaming velocity, and redshift, *Astrophys. J.* **917**, 40 (2021).
- [166] G. L. Bryan *et al.* (ENZO Collaboration), Enzo: An adaptive mesh refinement code for astrophysics, *Astrophys. J. Suppl. Ser.* **211**, 19 (2014).
- [167] R. K. Sheth and G. Tormen, Large scale bias and the peak background split, *Mon. Not. R. Astron. Soc.* **308**, 119 (1999).
- [168] D. Pequignot, P. Petitjean, and C. Boisson, Total and effective radiative recombination coefficients, *Astron. Astrophys.* **251**, 680 (1991).
- [169] D. Baumann, *Cosmology* (Cambridge University Press, Cambridge, England, 2022).
- [170] W. R. Inc., *Mathematica*, Version 13.3, Champaign, IL, 2023.
- [171] S. I. Grachev, Diffusion of resonance radiation in an infinite uniformly expanding medium, *Astrofizika* **30**, 347 (1989).
- [172] S. Furlanetto and J. R. Pritchard, The scattering of Lyman-series photons in the intergalactic medium, *Mon. Not. R. Astron. Soc.* **372**, 1093 (2006).
- [173] R. Barkana, The rise of the first stars: Supersonic streaming, radiative feedback, and 21-cm cosmology, *Phys. Rep.* **645**, 1 (2016).